

## THE STRONGEST MAGNETIC FIELDS ON THE COOLEST BROWN DWARFS

MELODIE M. KAO,<sup>1</sup> GREGG HALLINAN,<sup>1</sup> J. SEBASTIAN PINEDA,<sup>2</sup> DAVID STEVENSON,<sup>3</sup> AND ADAM BURGASSER<sup>4</sup>

<sup>1</sup> California Institute of Technology, Department of Astronomy, 1200 E California Blvd, MC 249-17, Pasadena, CA 91125, USA

<sup>2</sup> University of Colorado Boulder, Laboratory for Atmospheric and Space Physics, 3665 Discovery Drive, Boulder CO 80303, USA

<sup>3</sup> California Institute of Technology, Division of Geological & Planetary Sciences, 1200 E California Blvd, MC 150-21, Pasadena, CA 91125, USA

<sup>4</sup> University of California San Diego, Center for Astrophysics and Space Sciences, 9500 Gilman Drive, MC 0424, La Jolla, CA 92093, USA

### ABSTRACT

We have used the Jansky VLA to observe a sample of 5 known aurorally emitting late L and T dwarfs ranging in age from  $\sim$ 0.2–3.4 Gyr. We observed each target for seven hours, extending to higher frequencies than previously attempted for objects in this sample. We establish proportionally higher limits on maximum surface magnetic field strengths while simultaneously placing constraints on rotation periods through detections of repeating pulses. Observations at 8–12 GHz yield measurements of 3.7–4.1 kG localized field strengths (corresponding to minimum mean surface fields between 2.7–2.9 kG) on four of our targets, including the archetypal cloud variable T2.5 dwarf SIMP J01365663+0933473 recently proposed to be a possible planetary-mass object in the Carina-Near moving group. We detect a circularly polarized radio pulse at 15–16.5 GHz for the T6.5 dwarf 2MASS 10475385+2124234, corresponding to a localized 5.6 kG field strength and minimum mean surface field of 4.0 kG. For the same object, we also tentatively detect a circularly polarized radio pulse at 16.5–18 GHz corresponding to a localized 6.2 kG field strength and minimum mean surface field of 4.4 kG. We measure rotation periods between  $\sim$ 1.44–2.88 hr for all targets, supporting i) the emerging consensus in convective dynamo models that rapid rotation may be important for producing strong dipole fields and/or ii) rapid rotation is a key ingredient for driving the current systems powering auroral radio emission. We do not detect a clear cutoff in the pulsed emission for any targets, which would correspond to a maximum local surface magnetic field strength. However, we do observe evidence of variable structure in the frequency-dependent timeseries of our targets on timescales shorter than a rotation period, suggesting a higher degree of variability in the current systems near the surfaces of brown dwarfs, where emission at the highest frequencies are expected to probe. Finally, we find that old brown dwarfs may generate fields as strong as young brown dwarfs.

*Keywords:* brown dwarfs — planets and satellites: aurorae — planets and satellites: magnetic fields — radio continuum: stars — stars: individual (2MASS 10430758+2225236, 2MASS 12373919+6526148, SDSS 04234858-0414035, SIMP J01365662+0933473) — stars: magnetic fields

## 1. INTRODUCTION

Characterizing magnetic fields in the coolest dwarfs and eventually exoplanets can provide valuable insight into the formation, emission, and evolution of planets through stars. For instance, they are key players in disk accretion onto pre-main-sequence T Tauri stars (Hartmann et al. 2016), affecting planet formation mechanisms. Plasma flow across magnetic field lines drive large-scale currents in brown dwarf and planetary systems, producing auroral emission that likely contributes to the optical and infrared variability traditionally attributed to atmospheric clouds (e.g. Artigau et al. 2009; Radigan et al. 2014; Hallinan et al. 2015; Badman et al. 2015; Kao et al. 2016). Magnetic fields have been invoked to explain fundamental properties such as inflated radii in planets and stars (Batygin & Stevenson 2010; Kervella et al. 2016). Finally, they can mitigate the erosion of planetary atmospheres from strong stellar winds and coronal mass ejections, a special concern for planets in the habitable zones of M dwarfs and young stars (Vidotto et al. 2013; Brain et al. 2015; Leblanc et al. 2015).

To characterize such magnetic fields, it is important to understand the physical principles driving field generation in fully convective objects, which remains an open question in dynamo theory. Applications of convective dynamos span a wide breadth of cases, including rocky planet inner cores, gas giant planets, brown dwarfs, and low-mass stars. Fully convective objects cannot rely on strong differential rotation occurring between radiative and convective zones to help drive their dynamos. However they still exhibit magnetic activity like H $\alpha$ , X-ray, and radio emission (e.g. Berger et al. 2001, 2005; McLean et al. 2012; Schmidt et al. 2015; Pineda et al. 2016), and kilogauss fields have been confirmed for M, L, and T dwarfs (e.g. Reiners & Basri 2007, 2009; Morin et al. 2010; Hallinan et al. 2006, 2007, 2008; Route & Wolczan 2012; Kao et al. 2016). Turbulence dissipates fossil fields within  $\sim$ 10–100 years (Chabrier & Küker 2006), implying that a dynamo must continuously regenerate these strong fields.

Efforts to elucidate magnetic behaviors of fully convective objects have included many fruitful investigations into the role of rotation. For instance, H $\alpha$  and X-ray emission are both tracers of hot chromospheres and coronae in F through mid-M stars heated in part by magnetic processes (Vernazza et al. 1981; Schmitt & Rosso 1988; Ulmschneider 2003). Rotation appears to affect such magnetic processes, as H $\alpha$  and X-ray emission scale with increasing surface rotation or decreasing

Rossby<sup>1</sup> number, which measures the effect of the Coriolis force in the inertial part of the fluid flow (the convective time derivative of velocity). At Ro  $\sim$  0.1, the activity-rotation scaling appears to saturate at a constant  $\log L_{X,\text{H}\alpha}/L_{\text{bol}}$  (McLean et al. 2012), indicating a possible saturation of the influence of rotation on dynamo activity in mid-M and earlier type dwarfs. However, the neutral atmospheres of dwarfs  $\gtrsim$ M7 may preclude magnetic heating processes of similar nature from occurring in the coolest brown dwarfs (Mohanty et al. 2002), underscoring the need for an alternative way to evaluate magnetism on the coolest brown dwarfs.

Indeed,  $\gtrsim$ M7 dwarfs exhibit systematically weaker H $\alpha$  emission while  $L_X/L_{\text{bol}}$  decreases with increasing  $v \sin i$  or decreasing Ro (Mohanty & Basri 2003; Reiners & Basri 2008, 2010; Berger et al. 2010; McLean et al. 2012), and the Güdel-Benz relation appears to break down for objects later than M7 due to a suppression of X-ray luminosities, even when taking activity-rotation saturation into account (Berger et al. 2010; Williams et al. 2014). Rather than relying on proxies for magnetic activity to test the role of rotation in fully convective magnetism, direct measurements would be more ideal.

Models explore how different parameters quantifying competing forces such as Lorentz, buoyancy, and Coriolis affect energy exchange mechanisms at play in the magnetohydrodynamics occurring in dynamo regions. These models observe various dependencies between global magnetic field behaviors such as field topologies, magnetic energy, and time variation to observable object parameters such as luminosity, rotation, and age (e.g., Browning 2008; Christensen et al. 2009; Yadav et al. 2016), and testing them requires a means to probe magnetism in the coolest objects. For instance, in a recent breakthrough, scaling laws derived from planetary dynamo calculations appear to be dominated by convected energy flux, quantified by bolometric luminosity, rather than rotation (Christensen & Aubert 2006). Excitingly, these laws appeared to be empirically consistent with the magnetic field strengths measured for fully convective stars (Christensen et al. 2009). However, this scaling relation could not be verified for an important class of fully convective objects, cool brown dwarfs, because the only existing means of measuring magnetic fields relied on the Zeeman broadening of atomic and molecular lines (e.g., Johns-Krull & Valenti 1996; Donati et al. 2006; Reiners & Basri 2007; Morin et al. 2010), which existing limitations in instrumentation and knowledge

<sup>1</sup> Quantified as Ro  $\sim$   $P/\tau_c$ , where  $P$  is the stellar rotation period and  $\tau_c$  is the convective turnover time.

of Landé factors preclude from extending to L and later dwarfs (Reiners & Basri 2006).

The unexpected detection of quiescent and flaring radio emission from the M9 brown dwarf LP 944-20 at 4.9 and 8.5 GHz with the Very Large Array at the beginning of this millennium violated the tightly correlated Güdel-Benz relation linking coronal heating and magnetic particle acceleration (Güdel & Benz 1993) and heralded an unexpected new window into brown dwarf magnetism (Berger et al. 2001). This discovery paved the way to the subsequent detection of rotationally modulated and highly circularly polarized radio pulses attributed to the electron cyclotron maser (ECM) instability (Hallinan et al. 2006, 2007), which is the same process driving auroral radio emissions in the magnetized Solar System planets (Zarka 1998).

The identification of auroral ECM emission from brown dwarfs was a crucial step to probing magnetic field strengths on the coolest brown dwarfs. For cool brown dwarfs with largely neutral atmospheres where collisions are negligible (the ratio of the plasma frequency to the electron cyclotron frequency is very small), emission occurs very near the electron cyclotron fundamental frequency  $\nu_{\text{MHz}} \sim 2.8 \times B_{\text{Gauss}}$  (Treumann 2006, and references therein). While it cannot provide detailed insight into global magnetic field properties and the absence of such emission does not necessarily imply the absence of strong magnetic fields, detections of auroral radio emission provide powerfully direct measurements of field strengths at emitting locations within the magnetosphere.

In contrast, magnetic field measurements from the Zeeman broadening of magnetically sensitive spectral lines can return filling factor and surface-averaged field strengths with  $\sim 15\%-30\%$  uncertainties (Valenti et al. 1995; Johns-Krull & Valenti 1996, 2000; Reiners & Basri 2007; Reiners 2012; Shulyak et al. 2010). Zeeman Doppler imaging adds the ability to spatially distinguish different regions of different field strengths and reconstruct surface field topologies by fitting spectropolarimetric observations to those synthetically generated from test magnetic maps. Structure of opposite polarity on scales smaller than a spatial resolution element can cancel out, so ZDI is preferentially sensitive to the largest scales (Reiners & Basri 2009; Yadav et al. 2015), with significant confusion between the dipole and quadrupole components, and  $\sim 10\%-30\%$  uncertainties in dipole energies (Morin et al. 2010). Observations only probing some and not all of the Stokes parameters are further constrained in their abilities to fully capture complex field topologies (Rosén et al. 2015).

While auroral radio emission is likely only sensitive to large-scale fields, a careful interpretation of the measurements allows for comparison to Zeeman broadening measurements and paves the way to extending observational tests of fully convective dynamos to the coolest brown dwarfs (Kao et al. 2016).

However, efficient detection of brown dwarf auroral radio emission eluded astronomers for over a decade, with an overall detection rate of just  $\sim 10\%$  in previous volume-limited surveys (Antonova et al. 2013; Route 2016). Moreover, only one detection out of  $\sim 60$  L6 or later targets had been achieved before 2016 (Route & Wolszczan 2012), seriously hindering the application of ECM emission to testing dynamos mechanisms in the mass and temperature gap between planets and stars. Yet, the unprecedented discovery of a T6.5 dwarf emitting at  $\sim 4$  GHz demonstrated that such emission could indeed extend to objects probing the substellar-planetary boundary (Route & Wolszczan 2012).

Unexpectedly strong  $\sim$ kilogauss magnetic fields measured on brown dwarfs with ECM emission belied initial interpretations of weak X-ray emission in radio-bright brown dwarfs as evidence of very weak fields, and in fact Mohanty et al. (2002) showed that the decoupling of magnetic fields from the neutral atmospheres of these cool brown dwarfs could explain the weak X-ray emission. Instead of coronal heating processes, recent studies link ECM emission to other tracers of Solar System auroral activity such as H $\alpha$  emission and optical broadband variability (Harding et al. 2013; Hallinan et al. 2015; Pineda et al. 2016), suggesting a new model for magnetic activity in the coolest brown dwarfs: auroral emission.

We previously developed and tested a selection strategy for identifying likely ECM-emitting brown dwarf candidates making use of the emerging connection between auroral emissions and ECM and selecting targets with known H $\alpha$  emission and/or optical/infrared variability (Kao et al. 2016). This selection strategy led to the detection of ECM emission in four out of five new L7-T6.5 brown dwarf pilot targets at 4-8 GHz, confirming  $>2.5$  kG magnetic fields. A subsequent study confirmed detectable levels of H $\alpha$  emission for all but one of these targets (Pineda et al. 2016).

The addition of this collection of radio brown dwarf magnetic field measurements to the single previous measurement from the T6.5 dwarf 2MASS 10475385+2124234 (Route & Wolszczan 2012; Williams & Berger 2015) represented the tightest observational constraints on fully convective dynamo theory to date. Comparisons of ECM-derived magnetic field measurements to Zeeman-based measurements tentatively suggested that

dynamics operating in the coolest brown dwarfs may in fact produce fields that differ from values predicted by the luminosity-driven Christensen et al. (2009) model.

Higher frequency measurements of these objects can provide yet tighter constraints, motivating this work. Observations of ECM auroral emissions in the Solar System planets demonstrate that the emission drops off at a cut-off frequency corresponding to the strength of the field near the surface of the object, when interactions with the atmosphere begin to interrupt ECM emission processes. The persistence of highly circularly polarized and pulsing emission in our targets throughout the previously observed 4–8 GHz bandwidth suggested that the emitting electrons were still traversing the magnetospheres of our targets toward increasing magnetic flux. A detection of a cutoff in the ECM emission would provide the tightest radio-derived constraints on brown dwarf magnetic fields, and in fact none has yet been detected in any brown dwarfs to date.

Finally, the rotational modulation of auroral ECM emission provides a means of measuring rotational periods and eventually testing dynamo models examining the role of rotation by observing our known auroral radio emitters for longer time blocks to achieve full rotational phase coverage. Previous studies verify that pulse periods are consistent with rotational broadening from spectral lines (Berger et al. 2005; Hallinan et al. 2006, 2008; Berger et al. 2009).

In this work, we present new 8–12 GHz and 12–18 GHz observations of targets detected in our previous 4–8 GHz pilot survey (§3, §4.1). We carefully trace the evolution of auroral ECM pulses through 1- or 1.5- GHz sub-bands (§4.2, §5.2) and measure rotation periods (§4.3). Finally, we comment on implications for dynamo theory (§5).

## 2. TARGETS

Our sample of targets are discussed in Kao et al. (2016) but is again summarized here with updated literature for completeness. All targets are known to emit ECM emission at 4–8 GHz (Kao et al. 2016).

**2MASS 10475385+2124234.** 2M1047 is a T6.5 dwarf with known weak  $[L_{H\alpha}/L_{\text{bol}}] \sim 5.5$  (Pineda et al. 2016) and was the first T-dwarf detected at radio frequencies (Route & Wolszczan 2012). The detected emission was highly circularly polarized ( $\gtrsim 72\%$ ) at 4.75 GHz. Follow-up observations detected both quiescent and ECM emission up to 10 GHz (Williams et al. 2013; Williams & Berger 2015), the latter of which was used to measure a  $\sim 1.77$  hr rotation period up through 10 GHz. We included 2M1047 in our pilot survey to examine long-term variability and detected both pulsed and quiescent emission through 8 GHz. Using  $H_2O$  and  $K/H$  indices,

Kao et al. (2016) derived  $T_{\text{eff}} = 869^{+35}_{-29}$  K,  $>0.026 M_{\odot}$  estimated mass, and  $>2.5$  Gyr age.

**SIMP J01365662+0933473.** SIMP0136 is a T2.5 dwarf well known for periodic ( $P = 2.3895 \pm 0.0005$  hr) and high-amplitude ( $>5\%$ )  $J$ - and  $K_s$ -band photometric variability (Artigau et al. 2009; Croll et al. 2016). High-amplitude infrared variability appears to occur at a higher rate in L/T transition dwarfs (Radigan et al. 2014; Radigan 2014) and has been attributed to the onset of patchy clouds (Marley et al. 2010; Apai et al. 2013; Burgasser et al. 2014; Radigan et al. 2014) to explain wavelength-dependent variability. No  $H\alpha$  emission has been detected down to  $[L_{H\alpha}/L_{\text{bol}}] < -6.6$  but it has anomalously strong Li I at  $\text{EW} = 6.6 \pm 1.0$  and  $7.8 \pm 1.0$  Å for two different nights and is the latest-type object with a clear lithium detection, indicative of a young age (Pineda et al. 2016). Kao et al. (2016) derived  $T_{\text{eff}} = 1089^{+62}_{-54}$ ,  $0.022^{+0.015}_{-0.012} M_{\odot}$  estimated mass, and  $0.6^{+1.1}_{-0.3}$  Gyr age. Recently, Gagné et al. (2017) reported that SIMP0136 may be a member of the  $\sim 200$  Myr-old Carina-Near moving group. Using an empirical measurement of its bolometric luminosity and the the Saumon & Marley (2008) models, they inferred  $R = 1.22 \pm 0.01 R_J$ , which together predicted  $T_{\text{eff}} = 1098 \pm 6$  K and  $M = 12.7 \pm 1.0 M_J$ . New  $v \sin i$  measurements and its photometric periodicity further constrained  $R > 1.01 \pm 0.02 R_J$  and  $M < 42.6^{+2.5}_{-2.4} M_J$ .

**2MASS J10430758+2225236.** 2M1043 is an unusually red L8 dwarf with previously reported tentative  $H\alpha$  emission (Cruz et al. 2007). Pineda et al. (2016) confirm  $[L_{H\alpha}/L_{\text{bol}}] = -5.8 \pm 0.2$  as well as a tentative Li I absorption line with  $\text{EW} = 10 \pm 3$  Å. Kao et al. (2016) derived  $T_{\text{eff}} = 1390 \pm 180$  K,  $0.011^{+0.011}_{-0.005} M_{\odot}$  estimated mass, and  $0.6^{+4.6}_{-0.3}$  Gyr age.

**2MASS J12373919+6526148.** 2M1237 is a T6.5 dwarf with anomalously hyperactive  $H\alpha$  emission at  $[L_{H\alpha}/L_{\text{bol}}] \sim -4.2$  (Burgasser et al. 2000, 2002, 2003; Liebert & Burgasser 2007) with conflicting evidence of  $J$ -band variability (Burgasser et al. 2002; Artigau et al. 2003). Kao et al. (2016) derived  $T_{\text{eff}} = 831^{+31}_{-27}$  K,  $>0.028 M_{\odot}$  estimated mass, and  $>3.4$  Gyr age.

**SDSS 04234858-0414035.** SDSS0423 is an L6/T2 binary with  $0''.16$  separation (Burgasser et al. 2005; Carson et al. 2011) and strong  $H\alpha$  emission ( $\text{EW} = 3$  Å) and Li I absorption ( $\text{EW} = 11$  Å) (Kirkpatrick et al. 2008). Pineda et al. (2016) confirm  $H\alpha$   $\text{EW} = 2.95 \pm 0.3$  Å and Li I  $\text{EW} = 11.1 \pm 0.4$  Å. It additionally exhibits  $J$ - and  $K$ -band but no  $I_c$  photometric variability (Enoch et al. 2003; Clarke et al. 2008; Wilson et al. 2014). Kao et al. (2016) derived  $T_{\text{eff}} = 1678^{+174}_{-137}$  K,  $0.015^{+0.021}_{-0.006} M_{\odot}$  estimated mass, and  $0.49^{+0.62}_{-0.17}$  Gyr age.

**Table 1.** Survey Targets

Object Name	Abbrev.	SpT	Parallax	Distance	$\mu_\alpha \cos \delta$	$\mu_\delta$	Notes	Ref.
					Name	(mas)	(pc)	(mas/yr)
2MASS 10475385+2124234	2M1047	T6.5	94.73 $\pm$ 3.81	10.56 $\pm$ 0.52	-1714 $\pm$ 7	-489 $\pm$ 4	H $\alpha$ , detected prior	1–8
SIMP J01365662+0933473	SIMP0136	T2.5	162.32 $\pm$ 0.89	6.139 $\pm$ 0.037	1222.70 $\pm$ 0.78	0.5 $\pm$ 1.2	IR var, no H $\alpha$ <sup>a</sup>	8–12
2MASS J10430758+2225236	2M1043	L8	...	16.4 $\pm$ 3.2	-134.7 $\pm$ 11.6	-5.7 $\pm$ 17.0	H $\alpha$ emission	8 13–15
2MASS J12373919+6526148	2M1237	T6.5	96.07 $\pm$ 4.78	10.42 $\pm$ 0.52	-1002 $\pm$ 8	-525 $\pm$ 6	H $\alpha$ , IR var? <sup>b</sup>	1 3 4 16–18
SDSS J04234858-0414035	SDSS0423	L7 <sup>c</sup>	65.93 $\pm$ 1.7	15.17 $\pm$ 0.39	-331 $\pm$ 49	76 $\pm$ 11	H $\alpha$ , IR var, binary <sup>c</sup>	8 19 19–27

<sup>a</sup>(8) reported upper limits  $[L_{H\alpha}/L_{bol}] < -6.6$ .

<sup>b</sup>(16) and (18) report conflicting evidence of  $J$ -band variability.

<sup>d</sup>Secondary is spectral type T2.5 at orbital separation 0''.16 (25, 26, 27).

**References**— (1) Burgasser et al. (1999); (2) Burgasser et al. (2006b); (3) Vrba et al. (2004); (4) Burgasser et al. (2003); (5) Route & Wolszczan (2012); (6) Williams et al. (2013); (7) Williams & Berger (2015); (8) Pineda et al. (2016); (9) Weinberger et al. (2016); (10) Artigau et al. (2006); (11) Artigau et al. (2009); (12) Apai et al. (2013); (13) Cruz et al. (2007); (14) Schmidt et al. (2010); (15) Miles-Páez et al. (2017); (16) Burgasser et al. (2002); (17) Burgasser et al. (2000); (18) Artigau et al. (2003); (19) Cruz et al. (2003); (20) Kirkpatrick et al. (2008); (21) Enoch et al. (2003); (22) Clarke et al. (2008); (23) Radigan et al. (2014); (24) Burgasser (2007); (25) Carson et al. (2011); (26) Burgasser et al. (2005); (27) Burgasser et al. (2006a)

### 3. OBSERVATIONS

We observed 4 objects with previous C-band (4–8 GHz) detections spanning spectral range L7.5–T6.5 at X-band (8–12 GHz) as well as one T6.5 object with a previous X-band detection at Ku-band (12–18 GHz) with the full VLA. We used the WIDAR correlator in 3-bit observing mode for 4 GHz or 6 GHz bandwidth observations with 2s integrations in 7-hour time blocks for 35 total program hours. Observations took place during May 2015 in BnA configuration. Table 1 and Table 2 summarize target properties and observations, respectively.

#### 3.1. Calibrations

For SIMP0136 and SDSS0423, we calibrated our measurement sets using standard VLA flux calibrators 3C48 and 3C147, respectively, and nearby phase calibrators. Flux calibrators were observed at the beginning and end of each observing block and interpolated. After initially processing raw measurement sets with the VLA Calibration Pipeline, we manually flagged remaining RFI. Strong time-dependent RFI resulted in  $\sim$ 71 minutes of data loss near the end of the observing block for SDSS0423. Typical full-bandwidth sensitivity at BnA configuration for 7-hour observing blocks ( $\sim$ 5.5 hours and  $\sim$ 4 hours on source) is 1.2  $\mu$ Jy and 2.1  $\mu$ Jy for X and Ku bands, respectively. Typical 3-bit observations reach an absolute flux calibration accuracy of  $\sim$ 5% by bootstrapping flux densities with standard VLA flux calibrators. To correct for flux errors resulting from gain phase

variation over our observing window, we alternated between target and phase calibrator integrations, with 15- and 6-minute cycle times for X and Ku bands, respectively. Our gain solutions varied slowly and smoothly over time and without any ambiguous phase wraps, suggesting that this source of error is negligible.

For 2M1047, 2M1043, and 2M1237, we observed the flux calibrator 3C295, which is typically recommended only for low-frequency observations in compact configurations. This calibrator was fully resolved at both X and Ku bands for our observations. For targets observed at X bands (2M1043 and 2M1237), we modified the VLA scripted pipeline to use A configuration 8.464 GHz and 11.064 GHz model images observed on 02/16/2016 by VLA staff to set flux levels and determine bandpass solutions. The emission from 3C295 is stable within 1% over 24–28 years for X and Ku bands (Perley & Butler 2013). Because the lobed structure of 3C295 is resolved at our observing frequencies and the VLA sky sensitivity fringes are wavelength-dependent, we expect there to be a discrepancy in flux densities bootstrapped using these different images of 3C295. To estimate the additional uncertainty in flux densities introduced by calibrating with 3C295, we compared the flux densities of each target’s phase calibrator as bootstrapped by the different model images of 3C295. We list these flux densities in Table 3. These comparisons suggest that the flux densities of 2M1043 and 2M1237 have an additional  $\sim$ 1–7% uncertainty. We repeated the same process for our Ku band target (2M1047) but instead used model images of

**Table 2.** Summary of observations

Object	Band	Obs.	Obs.	Time on	VLA	Synthesized Beam	Phase	Flux	Ref. Set	
		(GHz)	Date	Block	Source	Configuration	Dimensions (arcsec $\times$ arcsec)	RMS ( $\mu$ Jy)	Calibrator	Calibrator
2M1047	12.0–18.0	05/18	7.0	20870	BnA	0''.62 $\times$ 0''.50	1.7 , 1.8	J1051+2119	3C295	14.064
SIMP0136	8.0–12.0	05/17	7.0	20870	BnA	0''.66 $\times$ 0''.37	1.3 , 1.1	J0149+0555	3C48	...
2M1043	8.0–12.0	05/20	7.0	20612	BnA	0''.60 $\times$ 0''.33	1.0 , 1.0	J1051+2119	3C295	11.064
2M1237	8.0–12.0	05/18	7.0	21484	BnA	0''.69 $\times$ 0''.43	1.0 , 1.1	J1339+6328	3C295	8.464
SDSS0423	8.0–12.0	05/30	7.0	17234	BnA	0''.68 $\times$ 0''.37	1.2 , 1.4	J0423-0120	3C147	...

**Table 3.** Comparison of phase calibrator flux densities

Object	Ref. Freq	Ref. Freq	Ref. Freq	Ref. Freq
	8.464 GHz (mJy)	11.064 GHz (mJy)	14.064 GHz (mJy)	16.564 GHz (mJy)
2M1047	...	...	603.7 $\pm$ 0.4	561.1 $\pm$ 0.2
2M1043	466.4 $\pm$ 1.2	469.0 $\pm$ 1.3	...	...
2M1237	173.3 $\pm$ 1.0	185.0 $\pm$ 1.0	...	...

3C295 at 14.064 GHz and 16.564 GHz, which we expect to introduce an additional  $\sim$ 8% uncertainty.

We flagged all data from 12–12.8 GHz during the first  $\sim$ 34 minutes of our target observing scans for 2M1047 due to strong RFI. After manually flagging remaining RFI, we average all of the measurements sets down in time from 2s integrations to 10s for faster processing.

### 3.2. Source Motion

We corrected the 2MASS coordinates (Skrutskie et al. 2006) of our targets using the proper motion measurements listed in Table 1 to obtain expected source positions. For the known binary SDSS0423, we did not correct for orbital motion because its 0''.16 orbital separation is well within the synthesized beam resolution.

## 4. RESULTS

### 4.1. Image Detections

We produced Stokes I and Stokes V images of each object (total and circularly polarized intensities, respectively) with the CASA `clean` routine, modeling the sky emission frequency dependence with one term and using natural weighting. Pixel sizes were 0''.04  $\times$  0''.04. We searched for a point source at the proper motion-corrected coordinates of each target. For our targets

**Table 4.** Summary of initial imaging detections

Object	RA	Dec	Stokes I	Stokes V	SNR
	(hh mm ss.ss)	(dd mm ss.ss)	( $\mu$ Jy)	( $\mu$ Jy)	( $\sigma$ )
2M1047	10 47 51.78	+21 24 14.90	21.9 $\pm$ 1.3	3.9 $\pm$ 1.5	16.8
SIMP0136	01 36 57.86	+09 33 47.00	85.7 $\pm$ 1.3	-23.8 $\pm$ 1.1	65.9
2M1043	10 43 07.44	+22 25 23.31	9.5 $\pm$ 1.0	-4.7 $\pm$ 1.0	9.5
2M1237	12 37 36.58	+65 26 05.70	35.0 $\pm$ 1.0	16.9 $\pm$ 1.2	35.0
SDSS0423	04 23 48.23	-04 14 02.15	15.4 $\pm$ 1.2	-0.5 $\pm$ 1.4	12.9

calibrated with 3C295, we selected a single calibrated measurement set as a reference set, noted in Table 4. We performed all subsequent reduction and analysis on this reference set.

We detected each of our five targets in Stokes I, with signal-to-noise ratios (SNR) ranging from 9.5–65.9 in the mean Stokes I flux density. Table 4 gives the measured mean flux density and rms noise of each source. Flux densities and source positions were determined by fitting an elliptical Gaussian point source to the cleaned image of each object at its predicted coordinates using the CASA task `imfit`.

### 4.2. Timeseries Pulse Detections & Magnetic Field Strengths

We used the `clean` routine to model all sources within a primary beam of our targets and subtract these sources from the UV visibility data using the CASA `uvsub` routine to prevent sidelobe contamination in our targets' timeseries. We then added phase delays to our visibility data using the CASA `fixvis` routine to place our targets at the phase center.

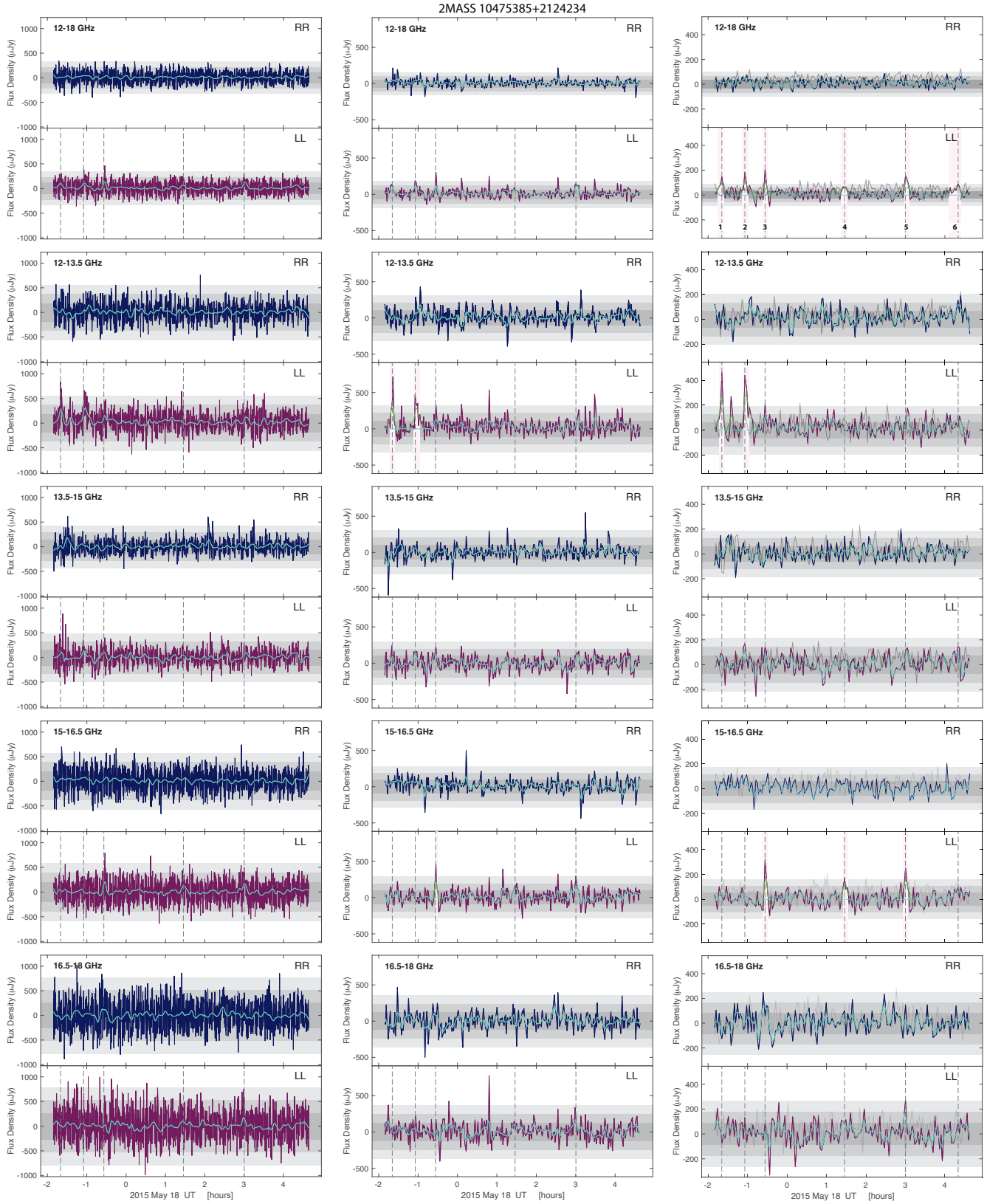


**Figure 1.** 10s, 60s, and 120s timeseries of rr- and ll-correlated (blue and maroon, respectively) flux densities for 2M1047 showing the emergence of apparent pulses at 12–13.5 GHz and 15–16.5 GHz. Green lines are smoothed timeseries used for identifying pulse candidates and overlaid cyan lines show removed pulse candidates for calculating rms noise and imaging quiescent emission. Light blue and pink bars highlight pulses identified by algorithm. Grey dashed lines are aligned to 12–13.5 GHz and 15–16.5 GHz pulse peaks. Grey regions indicates  $1\sigma$ ,  $2\sigma$ , and  $3\sigma$  rms noise. Comparison timeseries of a nearby object are plotted in dark grey in the 120s column.

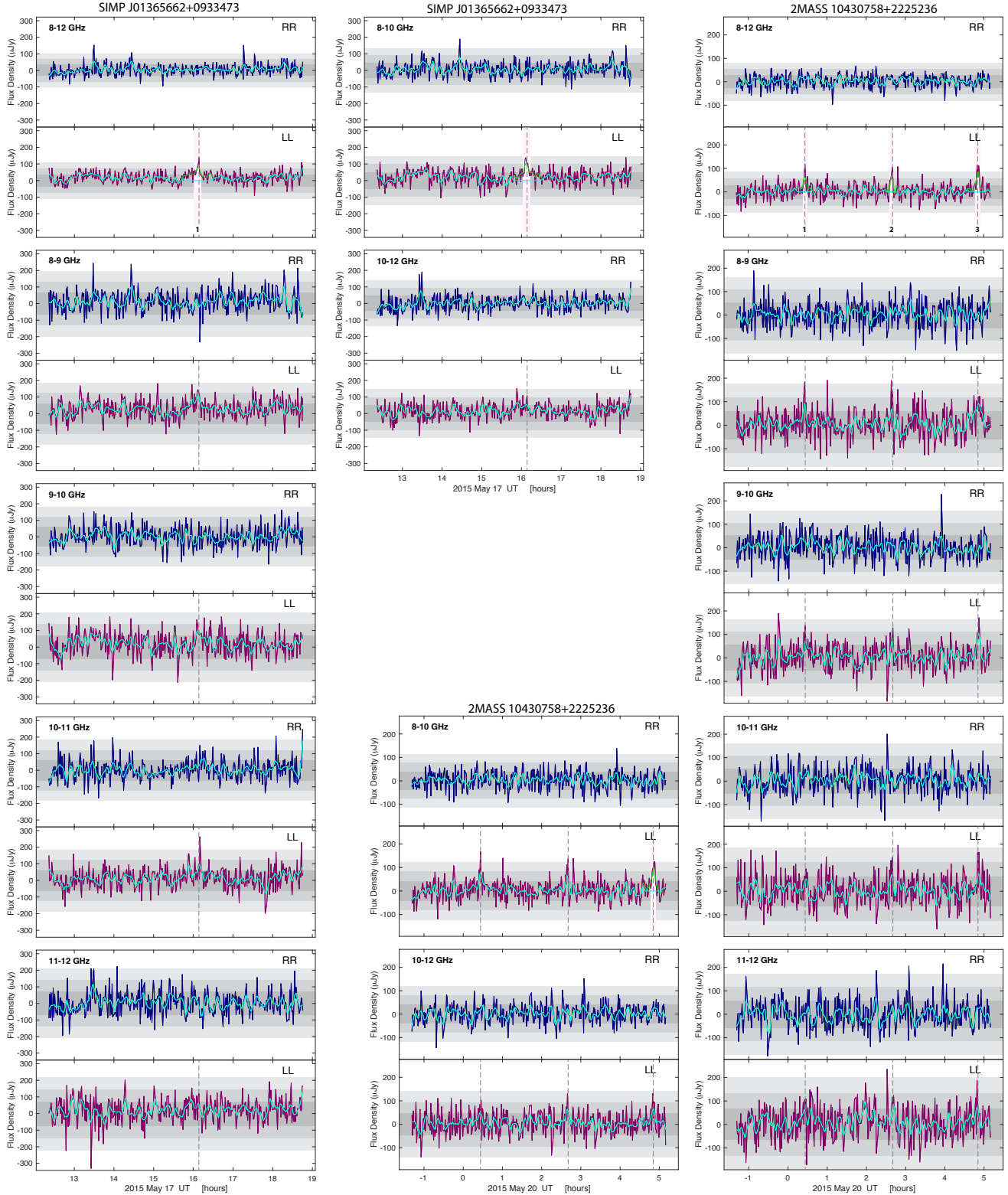


**Figure 2.** 60s timeseries of rr- and ll-correlated (blue and maroon, respectively) flux densities for SIMP0136 and 2M1043. Green lines are smoothed timeseries used for identifying pulse candidates and overlaid cyan lines show removed pulse candidates for calculating rms noise and imaging quiescent emission. Light blue and pink bars highlight pulses identified by algorithm. Grey dashed lines are aligned to pulse peaks. Grey regions indicates  $1\sigma$ ,  $2\sigma$ , and  $3\sigma$  rms noise.

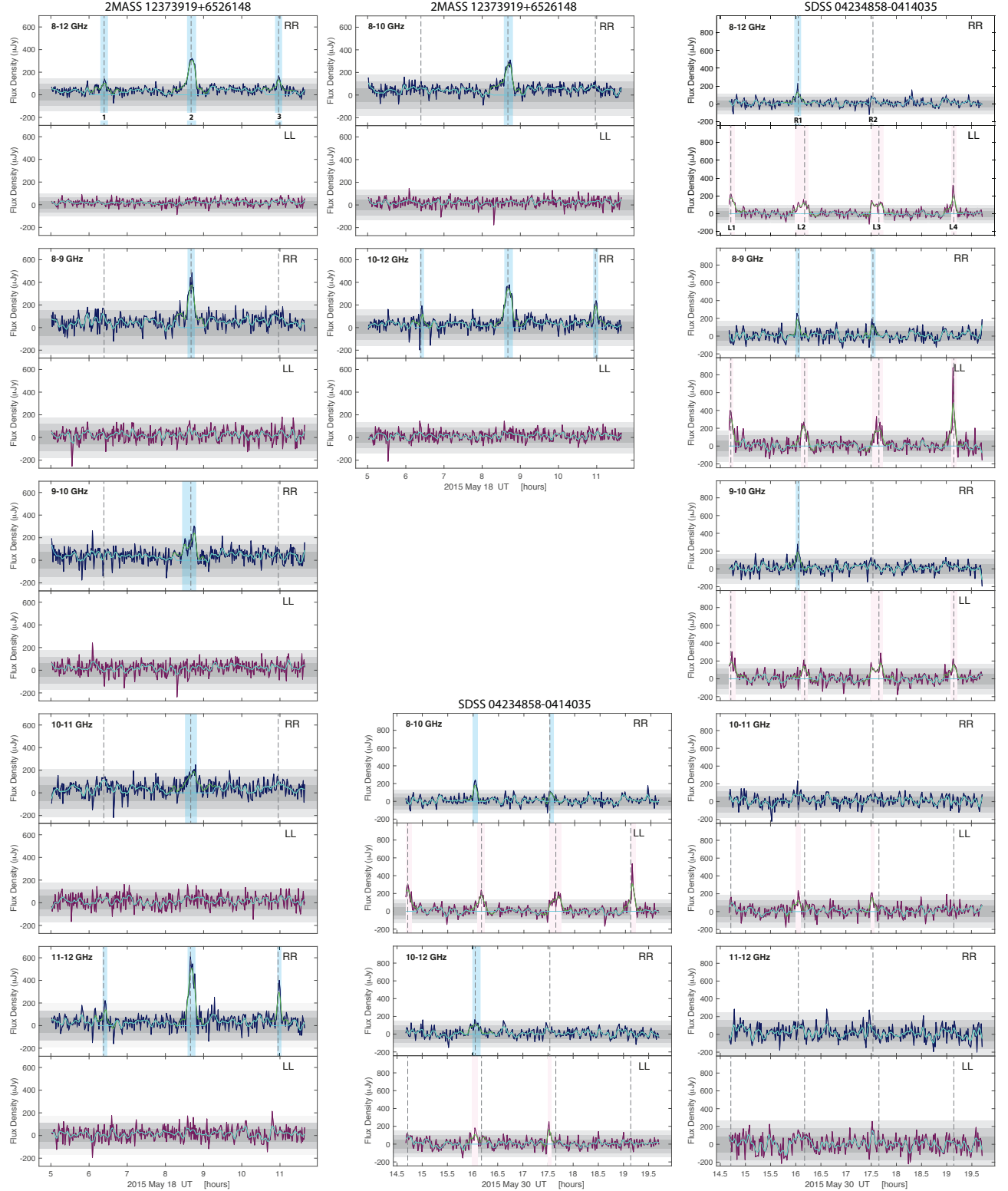


**Figure 3.** 60s timeseries of rr- and ll-correlated (blue and maroon, respectively) flux densities for 2M1237 and SDSS0423. Green lines are smoothed timeseries used for identifying pulse candidates and overlaid cyan lines show removed pulse candidates for calculating rms noise and imaging quiescent emission. Light blue and pink bars highlight pulses identified by algorithm. Grey dashed lines are aligned to pulse peaks. Grey regions indicates  $1\sigma$ ,  $2\sigma$ , and  $3\sigma$  rms noise.

**Table 5.** 2M1047: Pulsed and Quiescent Emission

		Pulse 1	Pulse 2	Pulse 3	Pulse 4	Pulse 5	Pulse 6	Pulses 4–6	Quiescent
<b>12–18GHz</b>									
Stokes I <sup>a</sup>	( $\mu$ Jy)	47.0 $\pm$ 14.8 <sup>c</sup>	50.7 $\pm$ 13.3	63.8 $\pm$ 12.9	<15.6	71 $\pm$ 11.6	31.0 $\pm$ 7.0	54.0 $\pm$ 7.1	7.4 $\pm$ 2.2 <sup>e</sup>
Stokes V <sup>a</sup>	( $\mu$ Jy)	-46.4 $\pm$ 14.3 <sup>c</sup>	<12.1	<14.9	<16.7	-56 $\pm$ 10.6	<6.5	-33.3 $\pm$ 8.3	<1.8
SNR	(I, V)	3.2, 3.2	3.8, ...	4.9, ...	...	6.1, 5.3	4.4, ...	7.6, 4.0	3.4, ...
Circ. Poln <sup>b</sup>	(%)	-90.2 $^{+38.3}_{-2.0}$	(-67.1 $^{+24.2}_{-20.0}$ )	(-67.3 $^{+24.0}_{-19.4}$ )	...	-76.8 $^{+16.8}_{-13.8}$	(-59.9 $^{+20.1}_{-23.4}$ )	-60.6 $^{+45.4}_{-39.0}$	...
<b>12–13.5GHz</b>									
Stokes I <sup>a</sup>	( $\mu$ Jy)	<30.5 <sup>c</sup>	143.4 $\pm$ 17.6	<28.2	<26.3	<27.0	<12.8	<16.1	20.4 $\pm$ 4.1 <sup>e</sup>
Stokes V <sup>a</sup>	( $\mu$ Jy)	-129.6 $\pm$ 24.6 <sup>c</sup>	-78.9 $\pm$ 21.7	<27.1	<25.9	<26.2	<16.1	<15.2	<4.1
SNR	(I, V)	..., 5.3	8.1, 3.6	...	...	...	...	...	5.0, ...
Circ. Poln <sup>b</sup>	(%)	(-72.8, -38.0)	-54.2 $^{+14.6}_{-18.8}$	...	...	...	...	...	...
<b>13.5–15GHz</b>									
Stokes I <sup>a</sup>	( $\mu$ Jy)	<35.0	<23.9	<26.8	<24.0	<24.1	<13.9	<14.7	<3.5
Stokes V <sup>a</sup>	( $\mu$ Jy)	<36.8	<22.8	<27.2	<25.3	<23.7	<13.6	<14.5	<3.7
SNR	(I, V)	...	...	...	...	...	...	...	...
Circ. Poln <sup>b</sup>	(%)	...	...	...	...	...	...	...	...
<b>15–16.5GHz</b>									
Stokes I <sup>a</sup>	( $\mu$ Jy)	<25.8	<22.1	125.4 $\pm$ 25.8	93.3 $\pm$ 19.9	93.7 $\pm$ 24.0	<12.9	105.2 $\pm$ 13.7	<4.1
Stokes V <sup>a</sup>	( $\mu$ Jy)	<25.9	<22.6	<28.2	<23.2	<21.3	<13.7	-46.7 $\pm$ 12.8	<4.0
SNR	(I, V)	...	...	4.9, ...	9.4, ...	3.9, ...	...	7.7, 3.6	...
Circ. Poln <sup>b</sup>	(%)	...	...	(-64.8 $^{+19.2}_{-20.8}$ )	(-71.4 $^{+26.5}_{-16.8}$ )	(-64.1 $^{+22.4}_{-21.8}$ )	...	-43.6 $^{+35.7}_{-50.9}$	...
<b>16.5–18GHz</b>									
Stokes I <sup>a</sup>	( $\mu$ Jy)	<33.1	<30.1	<34.3	<30.4	91.5 $\pm$ 28.7 <sup>d</sup>	<18.0	<19.1	<5.2
Stokes V <sup>a</sup>	( $\mu$ Jy)	<36.2	<29.6	<31.7	<33.3	-94.9 $\pm$ 24.9 <sup>d</sup>	<17.6	<18.8	<5.2
SNR	(I, V)	...	...	...	...	3.2, 3.8	...	...	...
Circ. Poln <sup>b</sup>	(%)	...	...	...	...	-58.0, -14.3	...	...	...

<sup>a</sup>Reported flux densities are integrated over the FWHM of the full-bandwidth 60s resolution data. Fixing fit parameters can result in overestimated uncertainties on the integrated and peak flux densities, so we report the rms image noise as the uncertainty  $\sigma_{\text{rms}}$ . For targets with a clear visual non-detection, we list  $\sigma_{\text{rms}}$ .

<sup>b</sup>Reported polarization fractions are highest-likelihood values, given the measured Stokes I and Stokes V flux densities. Uncertainties reflect upper and lower bounds of 68.27% confidence intervals. Negative and positive values indicate left and right circular polarizations, respectively. Upper-bound 68.27% and 99.73% confidence intervals are given for sub-bands with -100% circular polarization. Lower bounds are given in parentheses for objects without detectable levels of Stokes V emission, assuming a  $3\sigma_{\text{rms}}$  flux density.

<sup>c</sup>Possible Stokes I point sources at the expected location of 2M1047 for 12–18 GHz and 12–13.5 GHz are not clearly distinguishable by eye from the noise in the image. For 12–18 GHz, the significance of the measured Stokes I and Stokes V flux densities bootstrapped from 10,000 trials in a  $2.7' \times 2.7'$  image are 99.24% and 99.32%, respectively. For 12–13.5 GHz, the measured flux density at the expected location for 2M1047 is 104.4 $\pm$ 30.5, with a bootstrapped significance of 99.92%. However, the Stokes V flux density may be statistically significant with a bootstrapped significance of  $\geq$ 99.99%. Although the Stokes V flux is higher than the measured flux for Stokes I, the discrepancy is within the rms noise. We classify these detections as tentative.

<sup>d</sup>Tentative detection. Bootstrapped significance is 99.29% (Stokes I only), 99.63% (Stokes I with acceptable percent circular polarization constrained to 99.73% confidence interval), and 99.99% (Stokes I with acceptable percent circular polarization constrained to 68.27% confidence interval). For additional discussion, see §4.2.

<sup>e</sup>Tentative detections. Possible Stokes I point sources are apparent at the expected location of 2M1047 for 12–18 GHz and 12–13.5 GHz, but they are not clearly distinguishable by eye from the rms noise image. Bootstrapped significance levels are 99.59% and 99.98%, respectively.

**Table 6.** SIMP0136 & 2M1043: Pulsed and Quiescent Emission

		SIMP0136		2M1043				
		Pulse 1	Quiescent	Pulse 1	Pulse 2	Pulse 3	All Pulses	Quiescent
<b>8–12 GHz</b>								
Stokes I <sup>a</sup>	( $\mu$ Jy)	51.5 $\pm$ 5.7	11.5 $\pm$ 1.2	40.8 $\pm$ 8.0	60.5 $\pm$ 7.4	51.5 $\pm$ 5.6	49.3 $\pm$ 4.2	<1.2
Stokes V <sup>a</sup>	( $\mu$ Jy)	-33.3 $\pm$ 5.9	-7.1 $\pm$ 1.2	-34.7 $\pm$ 8.3	<8.2	-36.5 $\pm$ 6.6	-30.3 $\pm$ 4.3	<1.2
SNR	(I, V)	9.0, 5.6	9.6, 5.9	5.1, 4.2	8.2	9.2, 5.5	11.7, 7.0	...
Circ. Poln <sup>b</sup>	(%)	-63.9 $^{+11.5}_{-15.5}$	-61.1 $^{+10.5}_{-14.4}$	-82.0 $^{+24.1}_{-10.0}$ (-40.1 $^{+13.0}_{-16.7}$ )	-70.0 $^{+13.2}_{-15.2}$	-61.0 $^{+8.9}_{-11.7}$	...	...
<b>8–10 GHz</b>								
Stokes I <sup>a</sup>	( $\mu$ Jy)	57.2 $\pm$ 8.6	20.9 $\pm$ 1.8	50.1 $\pm$ 11.2	54.8 $\pm$ 9.3	55.1 $\pm$ 8.6	55.9 $\pm$ 5.8	<1.6
Stokes V <sup>a</sup>	( $\mu$ Jy)	-34.9 $\pm$ 8.1 <sup>c</sup>	-8.1 $\pm$ 1.8	-48.7 $\pm$ 10.9	<11.2	-48.7 $\pm$ 9.0	-44.3 $\pm$ 5.9	<1.6
SNR	(I, V)	6.7, 4.3	11.6, 4.5	4.5, 4.5	5.9, ...	6.4, 5.4	9.6, 7.5	...
Circ. Poln <sup>b</sup>	(%)	-59.7 $^{+13.8}_{-19.4}$	-38.5 $^{+8.5}_{-10.2}$	-92.7 $^{+29.8}_{-1.3}$ (-59.6 $^{+19.9}_{-22.1}$ )	-86.3 $^{+20.6}_{-7.3}$	-78.4 $^{+11.8}_{-12.0}$	...	...
<b>10–12 GHz</b>								
Stokes I <sup>a</sup>	( $\mu$ Jy)	40.5 $\pm$ 8.5 <sup>d</sup>	<2.1	<10.9	58.9 $\pm$ 11.6	44.0 $\pm$ 8.5	42.1 $\pm$ 5.7	<1.7
Stokes V <sup>a</sup>	( $\mu$ Jy)	<9.9	<1.6	<11.1	<11.9	<10.1	<6.0	<1.6
SNR	(I, V)	4.7, ...	...	...	5.1, ...	5.2, ...	7.4, ...	...
Circ. Poln <sup>b</sup>	(%)	(-70.3 $^{+25.8}_{-17.6}$ )	...	...	(-58.4 $^{+19.4}_{-23.2}$ )	(-66.4 $^{+23.4}_{-19.8}$ )	(-42.0 $^{+13.5}_{-18.2}$ )	...
<b>8–9 GHz</b>								
Stokes I <sup>a</sup>	( $\mu$ Jy)	69.9 $\pm$ 12.9	20.2 $\pm$ 2.1	43.4 $\pm$ 17.5	<15.9	59.3 $\pm$ 12.6	53.0 $\pm$ 9.0	<2.4
Stokes V <sup>a</sup>	( $\mu$ Jy)	<12.7	-7.5 $\pm$ 2.0	-67.1 $\pm$ 15.8	<16.4	-51.1 $\pm$ 11.8	-51.5 $\pm$ 8.1	<3.4
SNR	(I, V)	5.4, ...	9.6, 3.8	4.1, 5.0	...	4.7, 4.3	5.9, 6.4	...
Circ. Poln <sup>b</sup>	(%)	(-52.7 $^{+17.0}_{-23.7}$ )	-36.7 $^{+9.6}_{-12.1}$	-73.0, -35.6	...	-82.5 $^{+24.0}_{-9.7}$	-94.5 $^{+22.9}_{-1.0}$	...
<b>9–10 GHz</b>								
Stokes I <sup>a</sup>	( $\mu$ Jy)	44.3 $\pm$ 12.2 <sup>d</sup>	13.2 $\pm$ 2.4	<15.0	57.7 $\pm$ 13.3 <sup>e</sup>	56.1 $\pm$ 12.0	59.7 $\pm$ 7.8	<2.3
Stokes V <sup>a</sup>	( $\mu$ Jy)	<13.2	-9.1 $\pm$ 2.1	<14.0	<15.3	-48.0 $\pm$ 13.5	-36.3 $\pm$ 8.5	<2.3
SNR	(I, V)	3.6, ...	5.5, 4.3	...	4.3, ...	4.7, 3.6	7.7, 4.3	...
Circ. Poln <sup>b</sup>	(%)	(-83.2 $^{+35.3}_{-7.7}$ )	-66.8 $^{+16.1}_{-19.2}$	...	(-75.6 $^{+29.4}_{-13.9}$ )	-81.9 $^{+28.3}_{-9.6}$	-59.8 $^{+13.9}_{-18.4}$	...
<b>10–11 GHz</b>								
Stokes I <sup>a</sup>	( $\mu$ Jy)	41.5 $\pm$ 12.0 <sup>d</sup>	<3.0	<16.1	<16.6	<13.8	40.1 $\pm$ 7.8	<2.3
Stokes V <sup>a</sup>	( $\mu$ Jy)	<11.3	<2.3	<14.9	<16.7	<14.3	<8.6	<2.3
SNR	(I, V)	3.5, ...	...	...	...	...	5.1, ...	...
Circ. Poln <sup>b</sup>	(%)	(-75.6 $^{+29.9}_{-14.0}$ )	...	...	...	...	(-62.0 $^{+21.1}_{-21.9}$ )	...
<b>11–12 GHz</b>								
Stokes I <sup>a</sup>	( $\mu$ Jy)	<14.6	<3.5	<16.0	<17.0	<15.4	<9.2	<2.5
Stokes V <sup>a</sup>	( $\mu$ Jy)	<14.7	<3.0	<16.9	<17.4	<14.6	<9.3	<2.4
SNR	(I, V)	...	...	...	...	...	...	...
Circ. Poln <sup>b</sup>	(%)	...	...	...	...	...	...	...

<sup>a</sup>Reported flux densities are integrated over the FWHM of the full-bandwidth 60s resolution data. Fixing fit parameters can result in overestimated uncertainties on the integrated and peak flux densities, so we report the rms image noise as the uncertainty  $\sigma_{\text{rms}}$ . For targets with a clear visual non-detection, we list  $\sigma_{\text{rms}}$ .

<sup>b</sup>Reported polarization fractions are highest-likelihood values, given the measured Stokes I and Stokes V flux densities. Uncertainties reflect upper and lower bounds of 68.27% confidence intervals. Negative and positive values indicate left and right circular polarizations, respectively. Upper-bound 68.27% and 99.73% confidence intervals are given for sub-bands with -100% circular polarization. Lower bounds are given in parentheses for objects without detectable levels of Stokes V emission, assuming a  $3\sigma_{\text{rms}}$  flux density.

<sup>c</sup>Tentative image detection (no clearly visually distinguishable Stokes V point source). Bootstrapped significance is 99.67%.

<sup>d</sup>Tentative image detection (no clearly visually distinguishable Stokes I point source). Bootstrapped significance is 99.66% (10–12 GHz), 98.78% (9–10 GHz), 98.80% (10–11 GHz).

<sup>e</sup>Tentative image detection (no clearly visually distinguishable Stokes I point source). Bootstrapped significance is 99.54%.

**Table 7.** 2M1237: Pulsed and Quiescent Emission

		Pulse 1	Pulse 2	Pulse 3	Quiescent
<b>8–12GHz</b>					
Stokes I <sup>a</sup>	( $\mu$ Jy)	41.3 $\pm$ 5.4	159.7 $\pm$ 5.3	61.0 $\pm$ 5.7	27.8 $\pm$ 1.3
Stokes V <sup>a</sup>	( $\mu$ Jy)	26.5 $\pm$ 6.4	127.3 $\pm$ 5.5	34.2 $\pm$ 4.6	9.7 $\pm$ 1.4
SNR	(I, V)	7.6, 4.1	30.1, 23.1	10.7, 7.4	21.4, 6.9
Circ. Poln <sup>b</sup>	(%)	63.1 $^{+18.5}_{-15.4}$	79.6 $^{+4.6}_{-4.1}$	55.6 $^{+10.8}_{-7.9}$	34.8 $^{+5.5}_{-5.1}$
<b>8–10GHz</b>					
Stokes I <sup>a</sup>	( $\mu$ Jy)	30.0 $\pm$ 9.1	151.5 $\pm$ 9.0	52.4 $\pm$ 7.3	32.5 $\pm$ 1.9
Stokes V <sup>a</sup>	( $\mu$ Jy)	<8.3	122.6 $\pm$ 7.8	<6.9	9.2 $\pm$ 1.9
SNR	(I, V)	3.3, ...	16.8, 15.7	7.2, ...	17.1, 4.8
Circ. Poln <sup>b</sup>	(%)	(76.2 $^{+13.4}_{-30.5}$ )	80.6 $^{+7.7}_{-6.3}$	(38.8 $^{+17.1}_{-12.4}$ )	28.2 $^{+6.4}_{-5.8}$
<b>10–12GHz</b>					
Stokes I <sup>a</sup>	( $\mu$ Jy)	44.4 $\pm$ 7.6	174.3 $\pm$ 9.1	71.3 $\pm$ 8.6	22.8 $\pm$ 1.8
Stokes V <sup>a</sup>	( $\mu$ Jy)	<8.0	144.1 $\pm$ 9.0	57.6 $\pm$ 7.5	10.2 $\pm$ 1.8
SNR	(I, V)	5.8, ...	19.2, 16.0	8.3, 7.7	12.7, 5.7
Circ. Poln <sup>b</sup>	(%)	(52.5 $^{+23.0}_{-17.0}$ )	82.4 $^{+7.2}_{-6.2}$	79.6 $^{+11.8}_{-12.4}$	44.5 $^{+9.6}_{-8.0}$
<b>8–9GHz</b>					
Stokes I <sup>a</sup>	( $\mu$ Jy)	<12.3	197.7 $\pm$ 11.5	57.0 $\pm$ 11.4	33.8 $\pm$ 2.7
Stokes V <sup>a</sup>	( $\mu$ Jy)	<12.2	145.6 $\pm$ 10.7	<10.0	11.5 $\pm$ 2.2 <sup>d</sup>
SNR	(I, V)	... ...	17.2, 13.6	5.0, ...	12.5, 5.2
Circ. Poln <sup>b</sup>	(%)	... ...	73.4 $^{+7.7}_{-6.2}$	(50.6 $^{+24.4}_{-16.1}$ )	33.8 $^{+7.8}_{-6.5}$
<b>9–10GHz</b>					
Stokes I <sup>a</sup>	( $\mu$ Jy)	<12.0	97.1 $\pm$ 10.9	<11.4	30.1 $\pm$ 2.2
Stokes V <sup>a</sup>	( $\mu$ Jy)	<11.7	94.5 $\pm$ 10.4	<12.3	<2.4
SNR	(I, V)	... ...	8.9, 9.1	... ...	13.7, ...
Circ. Poln <sup>b</sup>	(%)	... ...	96.1 $^{+0.6}_{-17.0}$	... ...	(23.8 $^{+8.6}_{-7.9}$ )
<b>10–11GHz</b>					
Stokes I <sup>a</sup>	( $\mu$ Jy)	54.4 $\pm$ 12.6	96.7 $\pm$ 12.2	45.0 $\pm$ 11.7 <sup>c</sup>	21.5 $\pm$ 2.5
Stokes V <sup>a</sup>	( $\mu$ Jy)	<10.3	76.3 $\pm$ 11.7	<11.9	11.7 $\pm$ 2.5
SNR	(I, V)	4.3, ...	7.9, 6.5	3.8, ...	8.6, 4.7
Circ. Poln <sup>b</sup>	(%)	(54.0 $^{+25.5}_{-17.4}$ )	77.7 $^{+12.9}_{-13.7}$	(74.4 $^{+14.8}_{-28.8}$ )	53.7 $^{+15.7}_{-11.4}$
<b>11–12GHz</b>					
Stokes I <sup>a</sup>	( $\mu$ Jy)	<12.1	269.8 $\pm$ 13.6	99.2 $\pm$ 10.9	22.6 $\pm$ 2.7
Stokes V <sup>a</sup>	( $\mu$ Jy)	<12.0	222.4 $\pm$ 12.6	86.4 $\pm$ 11.2	9.6 $\pm$ 2.7 <sup>d</sup>
SNR	(I, V)	... ...	19.8, 17.7	9.1, 7.7	8.4, 3.6
Circ. Poln <sup>b</sup>	(%)	... ...	82.2 $^{+6.8}_{-5.7}$	86.1 $^{+8.0}_{-14.2}$	41.9 $^{+15.2}_{-11.5}$

<sup>a</sup>Reported flux densities are integrated over the FWHM of the full-bandwidth 60s resolution data. Fixing fit parameters can result in overestimated uncertainties on the integrated and peak flux densities, so we report the rms image noise as the uncertainty  $\sigma_{\text{rms}}$ . For targets with a clear visual non-detection, we list  $\sigma_{\text{rms}}$ .

<sup>b</sup>Reported polarization fractions are highest-likelihood values, given the measured Stokes I and Stokes V flux densities. Uncertainties reflect upper and lower bounds of 68.27% confidence intervals. Negative and positive values indicate left and right circular polarizations, respectively. Lower-bound 68.27% and 99.73% confidence intervals are given for sub-bands with 100% circular polarization. Upper bounds are given in parentheses for objects without detectable levels of Stokes V emission, assuming a  $3\sigma_{\text{rms}}$  flux density.

<sup>c</sup>Tentative image detection (no clearly visually distinguishable Stokes I point source). Bootstrapped significance is 99.20%.

<sup>d</sup>Tentative image detection (no clearly visually distinguishable Stokes V point source). Possible Stokes V point sources are apparent at the expected location of 2M1237 but are not clearly distinguishable by eye from the noise in the image. Bootstrapped significance is 99.93% (8–9 GHz) and 99.39% (11–12 GHz).

We checked all targets for highly circularly polarized flux density pulses to confirm the presence of ECM emission. Rather than searching for pulsed emission in Stokes I and V, we elected to search for pulses in the rr and ll correlations (right- and left-circularly polarized, respectively), where signal to noise is a factor of  $\sqrt{2}$  higher in cases where the pulsed emission is 100% circularly polarized, as is expected in an ideal case of ECM emission.

Using the CASA plotting routine `plotms` to export the real UV visibilities averaged across all baselines, channels, and spectral windows of the rr and ll correlations at 10s, 60s, and 120s time resolutions, we created rr and ll timeseries for all X-band targets at 8–9 GHz, 9–10 GHz, 10–11 GHz, 11–12 GHz, 8–10 GHz, 10–12 GHz, and 8–12 GHz bandwidths to check for frequency-dependent ECM emission cutoff. We repeat the same procedure for 2M1047 but divide the total bandwidth into 12–13.5 GHz, 13.5–15 GHz, 15–16.5 GHz, 16.5–18 GHz, 12–15 GHz, 15–18 GHz, and 12–18 GHz. Figures 1, 2, and 3 show the timeseries for each object.

We identify pulses using the following method: we smooth each timeseries with a locally weighted first degree polynomial regression (LOESS) and a smoothing window of 2.5% of the on-target time to prevent anomalous noise spikes, typically very narrow with  $\sim$ single time resolution element widths, from erroneously being identified as a pulse while also preventing the smearing out of slightly wider legitimate pulses. We then identify  $2\sigma$  outlier peaks in the smoothed timeseries and measure the full width half maximum (FWHM) of the smoothed pulse, where we use the rms of the timeseries as a proxy for any quiescent emission. In reality, these peaks lie above twice the quiescent emission, since the rms includes the peaks. Approximating each pulse as Gaussian, we define the full width of each pulse as three times the FWHM and remove each pulse from the raw timeseries. These initial steps remove the strongest pulses present in the timeseries that may cause weaker pulses from being automatically identified. Finally, we repeat the process once more to identify any other pulse candidates. Because sensitivity can be a concern at narrow time resolutions and bandwidths in the timeseries, we elected to conservatively set the detection threshold for this second iteration at  $2\sigma$  and separately verify the pulses by imaging each candidate pulse in Stokes I and V and comparing flux densities with that of the non-pulsed (quiescent) emission.

Highly circularly polarized pulses are clearly evident in the 10s, 60s, and 120s sub-band timeseries for 2M1047, 2M1237, and SDSS0423. For 2M1043, pulses do not become clearly evident until the data are aver-

aged across the full 8–12 GHz bandwidth. In contrast, SIMP0136 appears to have broadly variable radio emission with a single broad peak that is persistent across 60s and 120s sub-band timeseries. Infrared cloud variability studies of SIMP0136 suggest that its rotation period is  $\sim$ 2.4 hr. This *a priori* knowledge of the expected pulse periodicity allows us to search for pulses at expected occurrence times in our observing block. A pulse occurring before the above-noted timeseries peak would have directly coincided with a phase calibrator observation and thus possibly prevented its detection. A pulse occurring after would have taken place near the middle of the target integration block, when phase errors would be greatest and may possibly smear out flux from a pulse. To check for the effects of phase errors on flux densities, we imaged a bright nearby object at  $01^{\text{h}}36^{\text{m}}47\text{s}63s +09^{\circ}34'04\text{.}25$  and well within the  $\sim$ 4.5'primary beam during ‘edge’ observing scans directly adjacent to a phase calibration scan and ‘middle’ scans that are sandwiched by the edge scans and therefore likely to suffer from the worst phase calibration errors. We measured only a  $3.2 \pm 1.8\%$  decrease in flux, suggesting that phase calibration errors cannot account for a possible missing pulse.

One of the 12–13.5 GHz pulses for 2M1047 occurs during the time range when strong RFI caused all 12–12.8 GHz data to be flagged, which affects noise properties. As a check, we additionally create timeseries for a nearby object at  $10^{\text{h}}47^{\text{m}}54\text{s}95 +21^{\circ}24'13\text{.}40\text{s}$  and search for correlated variability, which we include in the 120s 2M1047 timeseries figures. This comparison object does not exhibit any evidence of highly circularly polarized pulses at any of the frequencies or timestamps associated with the pulses detected for 2M1047.

We confirm pulses with Stokes I and V imaging over the 60s FWHM of each pulse and measuring integrated Stokes I and Stokes V flux densities using the CASA routine `imfit`. In an initial set of fits, we allow the peak location to float and fix the semi-major and semi-minor axes to the dimensions of a synthesized beam, and our fitting region is a  $100 \times 100$  pixel region centered at the target location measured in §4.1. We select the highest signal-to-noise pulse as a benchmark and perform a second iteration of fits while also holding the benchmark peak location constant. We list measurements for pulses with unambiguous imaging and rms noise limits for frequency sub-bands with no detection. Imaging for some sub-bands show evidence for a possible point source at the expected target location that is not clearly distinguishable by eye from the noise in the image. We classify flux density measurements for these sub-bands as tentative detections and bootstrap the significance of

**Table 8.** SDSS0423: Pulsed and Quiescent Emission

		Pulse R1	Pulse R2	Pulse L1	Pulse L2	Pulse L3	Pulse L4	Quiescent
<b>8–12GHz</b>								
Stokes I <sup>a</sup>	( $\mu$ Jy)	86.9 $\pm$ 9.6	82.0 $\pm$ 9.5	99.2 $\pm$ 8.2	58.0 $\pm$ 6.6	64.6 $\pm$ 5.0	101.0 $\pm$ 9.1	<1.7
Stokes V <sup>a</sup>	( $\mu$ Jy)	<9.9	<8.0	-94.2 $\pm$ 6.7	-37.0 $\pm$ 7.0	-34.3 $\pm$ 4.6	-99.3 $\pm$ 10.1	<1.9
SNR	(I, V)	9.1, ...	8.6, ...	12.1, 14.1	10.1, 7.6	12.9, 7.5	11.1, 9.8	...
Circ. Poln <sup>b</sup>	(%)	(33.8 $^{+13.5}_{-11.0}$ )	(28.9 $^{+11.8}_{-9.4}$ )	-94.3 $^{+10.9}_{-2.8}$	-63.0 $^{+12.1}_{-16.0}$	-52.8 $^{+7.4}_{-9.3}$	-81.8, -62.2	...
<b>8–10GHz</b>								
Stokes I <sup>a</sup>	( $\mu$ Jy)	90.2 $\pm$ 11.4	96.5 $\pm$ 10.6	121.4 $\pm$ 11.7	69.3 $\pm$ 8.7	82.6 $\pm$ 6.0	152.6 $\pm$ 13.3	<2.2
Stokes V <sup>a</sup>	( $\mu$ Jy)	51.9 $\pm$ 10.9	<11.5	-132.3 $\pm$ 12.5	-67.1 $\pm$ 9.8	-49.6 $\pm$ 6.0	-151.9 $\pm$ 15.8	<2.2
SNR	(I, V)	7.9, 4.8	9.1, ...	10.4, 10.6	8.0, 6.8	13.8, 8.3	11.5, 9.6	...
Circ. Poln <sup>b</sup>	(%)	56.6 $^{+16.8}_{-11.8}$	(35.3 $^{+14.1}_{-11.5}$ )	-86.4, -68.0	-95.3 $^{+20.6}_{-0.7}$	-59.7 $^{+7.6}_{-9.6}$	-82.3, -62.5	...
<b>10–12GHz</b>								
Stokes I <sup>a</sup>	( $\mu$ Jy)	83.7 $\pm$ 14.5	56.5 $\pm$ 13.8	67.2 $\pm$ 12.9 <sup>d</sup>	<10.5	53.1 $\pm$ 8.8	<13.9	<2.4
Stokes V <sup>a</sup>	( $\mu$ Jy)	<13.3	<13.0	<12.5	<10.1	<7.8	<15.3	<2.5
SNR	(I, V)	5.8, ...	4.1, ...	5.2, ...	...	6.0, ...	...	...
Circ. Poln <sup>b</sup>	(%)	(46.3 $^{+22.2}_{-14.7}$ )	(65.2 $^{+21.0}_{-23.0}$ )	(-53.8 $^{+17.4}_{-24.0}$ )	...	(-42.9 $^{+42.9}_{-55.4}$ )	...	...
<b>8–9GHz</b>								
Stokes I <sup>a</sup>	( $\mu$ Jy)	73.8 $\pm$ 18.5	111.6 $\pm$ 14.0	133.5 $\pm$ 16.3	72.2 $\pm$ 12.9	95.5 $\pm$ 8.9	218.1 $\pm$ 21.0	<2.8
Stokes V <sup>a</sup>	( $\mu$ Jy)	65.7 $\pm$ 16.0 <sup>c</sup>	<14.7	-166.7 $\pm$ 16.1	-78.5 $\pm$ 13.7	-52.8 $\pm$ 9.1	-209.9 $\pm$ 21.0	<2.8
SNR	(I, V)	4.0, 4.1	8.0, ...	8.2, 10.4	5.6, 5.7	10.7, 5.8	10.4, 10.0	...
Circ. Poln <sup>b</sup>	(%)	83.9 $^{+8.3}_{-26.6}$	(38.9 $^{+16.4}_{-12.6}$ )	-88.4, -70.2	-73.4, -42.1	-54.8 $^{+9.5}_{-12.5}$	-95.4 $^{+14.8}_{-1.5}$	...
<b>9–10GHz</b>								
Stokes I <sup>a</sup>	( $\mu$ Jy)	110.2 $\pm$ 19.0	93.6 $\pm$ 14.8	102.3 $\pm$ 15.9	60.6 $\pm$ 12.0	69.6 $\pm$ 8.8	86.5 $\pm$ 18.2	<2.9
Stokes V <sup>a</sup>	( $\mu$ Jy)	<18.2	<15.6	-103.3 $\pm$ 15.3	-56.5 $\pm$ 12.4	-49.8 $\pm$ 8.5	-107.0 $\pm$ 21.0	<2.9
SNR	(I, V)	5.8, ...	6.3, ...	6.4, 6.8	5.0, 4.6	7.9, 5.9	4.8, 5.1	...
Circ. Poln <sup>b</sup>	(%)	(48.1 $^{+22.6}_{-15.3}$ )	(48.8 $^{+21.8}_{-15.7}$ )	-74.7, -47.8	-89.8 $^{+62.8}_{-10.2}$	-70.4 $^{+12.8}_{-15.6}$	-72.9, -36.8	...
<b>10–11GHz</b>								
Stokes I <sup>a</sup>	( $\mu$ Jy)	82.7 $\pm$ 17.9	<17.6	<16.5	<13.0	<10.5	<21.9	<2.8
Stokes V <sup>a</sup>	( $\mu$ Jy)	<19.0	<16.3	<16.0	<12.9	<10.1	<20.1	<2.8
SNR	(I, V)	4.6, ...	...	...	...	...	...	...
Circ. Poln <sup>b</sup>	(%)	(65.9 $^{+20.3}_{-23.3}$ )	...	...	...	...	...	...
<b>11–12GHz</b>								
Stokes I <sup>a</sup>	( $\mu$ Jy)	<23.8	<22.0	<29.4	<17.1	<13.3	<25.1	<4.3
Stokes V <sup>a</sup>	( $\mu$ Jy)	<24.2	<21.9	<32.4	<17.1	<12.7	<25.5	<5.4
SNR	(I, V)	...	...	...	...	...	...	...
Circ. Poln <sup>b</sup>	(%)	...	...	...	...	...	...	...

<sup>a</sup>Reported flux densities are integrated over the FWHM of the full-bandwidth 60s resolution data. Fixing fit parameters can result in overestimated uncertainties on the integrated and peak flux densities, so we report the rms image noise as the uncertainty  $\sigma_{\text{rms}}$ . For targets with a clear visual non-detection, we list  $\sigma_{\text{rms}}$ .

<sup>b</sup>Reported polarization fractions are highest-likelihood values, given the measured Stokes I and Stokes V flux densities. Uncertainties reflect the upper and lower bounds of the 68.27% confidence intervals. Negative and positive values indicate left and right circular polarizations, respectively. Lower-bound 68.27% and 99.73% confidence intervals are given for objects with 100% circular polarization. For pulses without detectable levels of Stokes V emission, we give upper bounds on the percent circular polarization in parentheses by assuming a  $3\sigma_{\text{rms}}$  flux density.

<sup>c</sup>Tentative image detection (no clearly visually distinguishable Stokes V point source). Bootstrapped significance is 99.27%.

<sup>d</sup>Tentative Stokes I image detection is difficult to distinguish from image noise. Bootstrapped significance is  $\geq$ 99.99%.

the possible point source by randomly drawing 10,000 pointings in a  $4096 \times 4096$  pixel ( $2.7' \times 2.7'$ ) image and measuring the flux densities for a point source centered on these pointings.

We calculate the highest likelihood percent circular polarization, where negative and positive percentages correspond to left and right circular polarizations, respectively. We report uncertainties that correspond to the upper and lower limits of the 68.27% confidence interval and record the evolution of pulse flux densities across sub-bands in Table 5 (2M1047), Table 6 (SIMP0136 & 2M1043), Table 7 (2M1237), and Table 8 (SDSS0423). Some pulses appear to have Stokes V fluxes that are higher than the Stokes I fluxes, which is not physically possible. However, these anomalous excess flux densities are within the rms noise. For objects with 100% circular polarization, we give the lower-bounds of the 68.27% and 99.73% confidence intervals on the circular polarization.

We additionally measure quiescent emission by removing the full width of each pulse across the entire 4- or 6-GHz bandwidth from our data and imaging the remaining emission, shown in Figure 4. Curiously, 2M1043 and SDSS0423 do not appear to have any detectable quiescent emission above  $\sim 3.6 \mu\text{Jy}$  or  $\sim 5.1 \mu\text{Jy}$  ( $3\sigma_{\text{rms}}$ ), respectively, for the full 8–12 GHz bandwidth. In contrast, the quiescent emission from SIMP0136 is unexpectedly highly circularly polarized at  $\sim 60\%$ . We report the characteristics of the pulsed and quiescent emission in Tables 5, 6, 7, and 8.

2M1043 and 2M1047 have very faint pulses that are difficult to individually distinguish by eye in the imaging. As a further check, we average these pulses together for each object to reduce rms noise in the image and report measured flux densities. For 2M1043, all of the pulses are clearly detectable in Stokes I through the 10–11 GHz band, in contrast to undetectable quiescent emission. For 2M1047, Pulses 4–6 were clearly detectable by eye in the 12–18 GHz and 15–16.5 GHz images. Additionally, Pulse 5 may extend into the 16.5–18 GHz timeseries. We measured Stokes I and Stokes V flux densities of  $91.5 \pm 28.7 \mu\text{Jy}$  and  $-94.9 \pm 24.9 \mu\text{Jy}$ , respectively. The percent circular polarization is expected to lie between  $[-100\%, -58.0\%]$  with 68.27% confidence and  $[-100\%, -14.3\%]$  with 99.73% confidence. However, there is not a clear point source in the associated images. The bootstrapped Stokes I significance is 99.29%. The significance increases to 99.63% and 99.99% when we constrain the acceptable percent circular polarization to lie within the 99.73% and 68.27% confidence intervals, respectively, so we classify the 16.5–18 GHz detection as a tentative detection.

### 4.3. Rotation Period Measurements

**Table 9.** Periodogram Results

Object	L-S (hr)	Plavchan (hr)	BLS (hr)	Adopted (hr)
2M1047	$0.59^{+0.02}_{-0.02}$	$1.78^{+0.07}_{-0.06}$	$1.77^{+0.05}_{-0.05}$	$1.78^{+0.07}_{-0.06}$
SIMP0136	$2.33^{+0.43}_{-0.32}$	$2.88^{+0.34}_{-0.27}$	$2.74^{+0.80}_{-0.50}$	$2.88^{+0.34}_{-0.27}$
2M1043	$2.36^{+0.42}_{-0.31}$	$2.19^{+0.15}_{-0.12}$	$2.21^{+0.14}_{-0.13}$	$2.21^{+0.14}_{-0.13}$
2M1237	$2.21^{+0.59}_{-0.39}$	$2.28^{+0.10}_{-0.09}$	$2.28^{+0.13}_{-0.12}$	$2.28^{+0.10}_{-0.09}$
SDSS0423	$1.44^{+0.19}_{-0.15}$	$1.49^{+0.11}_{-0.10}$	$1.47^{+0.13}_{-0.11}$	$1.47^{+0.13}_{-0.11}$

Magnetic dynamos act essentially by converting available energy into magnetic energy. One potential source of energy is the kinetic energy provided by rotation.

Differential rotation can shear poloidal fields into a toroidal field, a process known as the  $\Omega$ -effect. In convective regions with limited or absent differential rotation, Coriolis forces from rotation can influence convective motions and therefore dependent dynamo mechanisms, for example by twisting rising and falling convection cells as in the  $\alpha$ -effect, which has been attributed to driving a poloidal field (Durney 1981; Noyes et al. 1984). Together, these two effects form the two-part  $\alpha\Omega$  dynamo, one long-standing model of a dynamo mechanism in higher-mass stars with a tachocline (Moffatt 1978; Steenbeck & Krause 1966; Charbonneau 2005). Such a dynamo may also occur to a lesser degree in cooler, fully convective objects such as when strong zonal flows in the molecular layers of an object penetrate into more conductive regions (e.g. Gastine et al. 2012; Duarte et al. 2013; Gastine et al. 2014; Duarte et al. 2016) or differential rotation arises even in objects without a tachocline (Browning 2008).

We briefly summarize modeling results here to provide context for understanding various ways that rotation may relate to potentially observable behaviors of magnetic fields generated by fully convective dynamos. Magnetic energies may increase with rotation rates up to a saturation level for  $\alpha^2$  dynamos (Chabrier & Küker 2006). In other models, field morphologies and their time variability may depend on the influence of rotation (e.g. Christensen & Aubert 2006; Sreenivasan & Jones 2006; Olson & Christensen 2006; Browning 2008; Yadav et al. 2016). Along similar lines, the onset of dipole-dominated fields in addition to multipole-dominated fields in an apparent bistable dynamo can occur as model parameters transition from higher to lower Rossby numbers indicating the strong influence of ro-

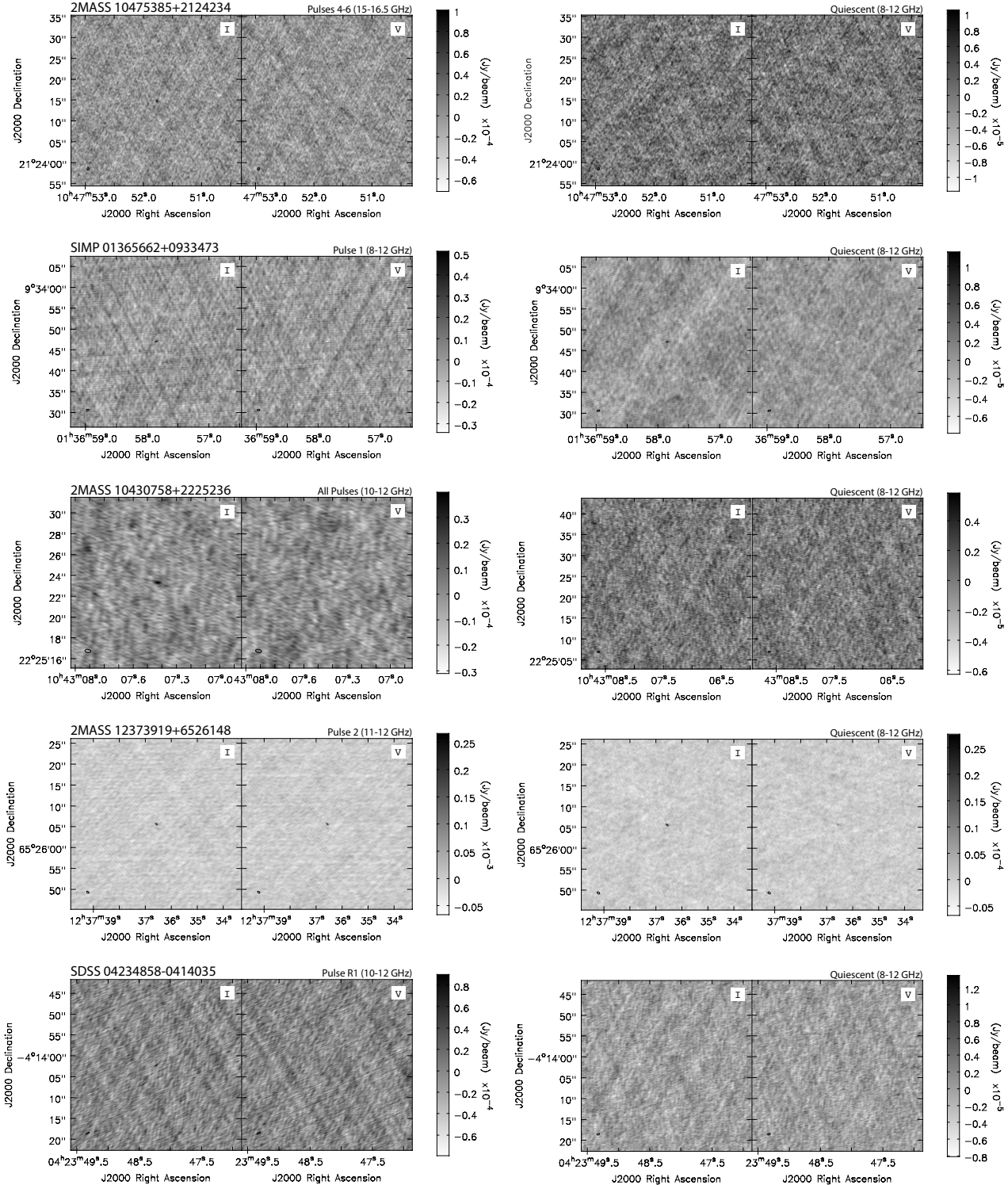


**Figure 4.** Stokes I and Stokes V images of pulsed emission (left) and quiescent emission (right). Images are centered over measured target coordinates and ellipses in bottom left corners depict synthesized beam dimensions. No quiescent emission is detectable from 2M1043 or SDSS0423. A measurement of the flux density at the expected coordinates for 2M1047 yields a tentative detection, but a point source is not clearly distinguishable by eye.

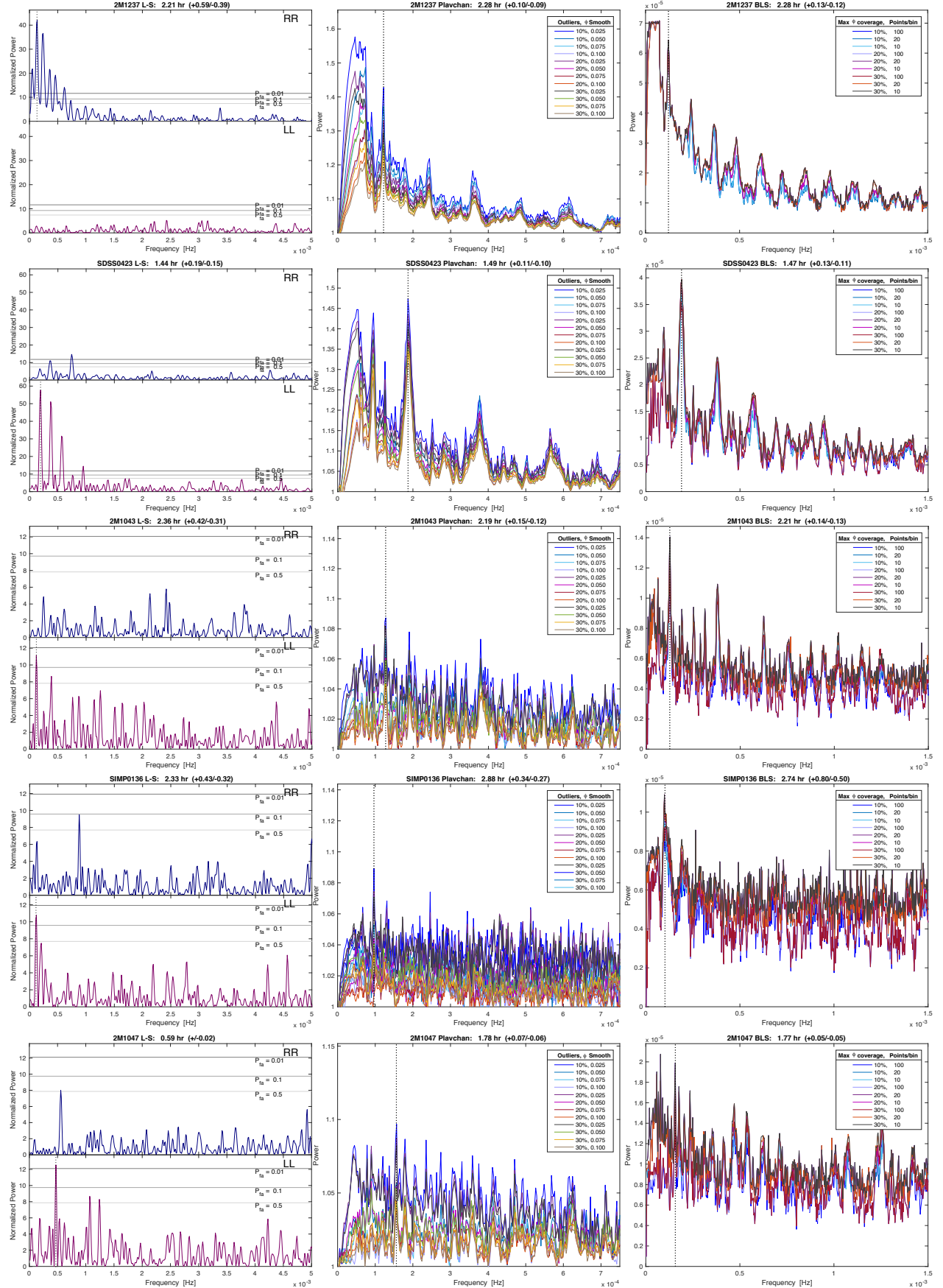


**Figure 5.** From left to right: Lomb-Scargle (L-S), Plavchan, and Box-fitting Least Squares (BLS) periodograms. RR and LL periodograms are shown for the L-S periodogram to show relative powers of peaks between timeseries with apparent periodic variation and ones without. Periodograms for Plavchan and BLS algorithms are for correlations with strongest L-S peaks.

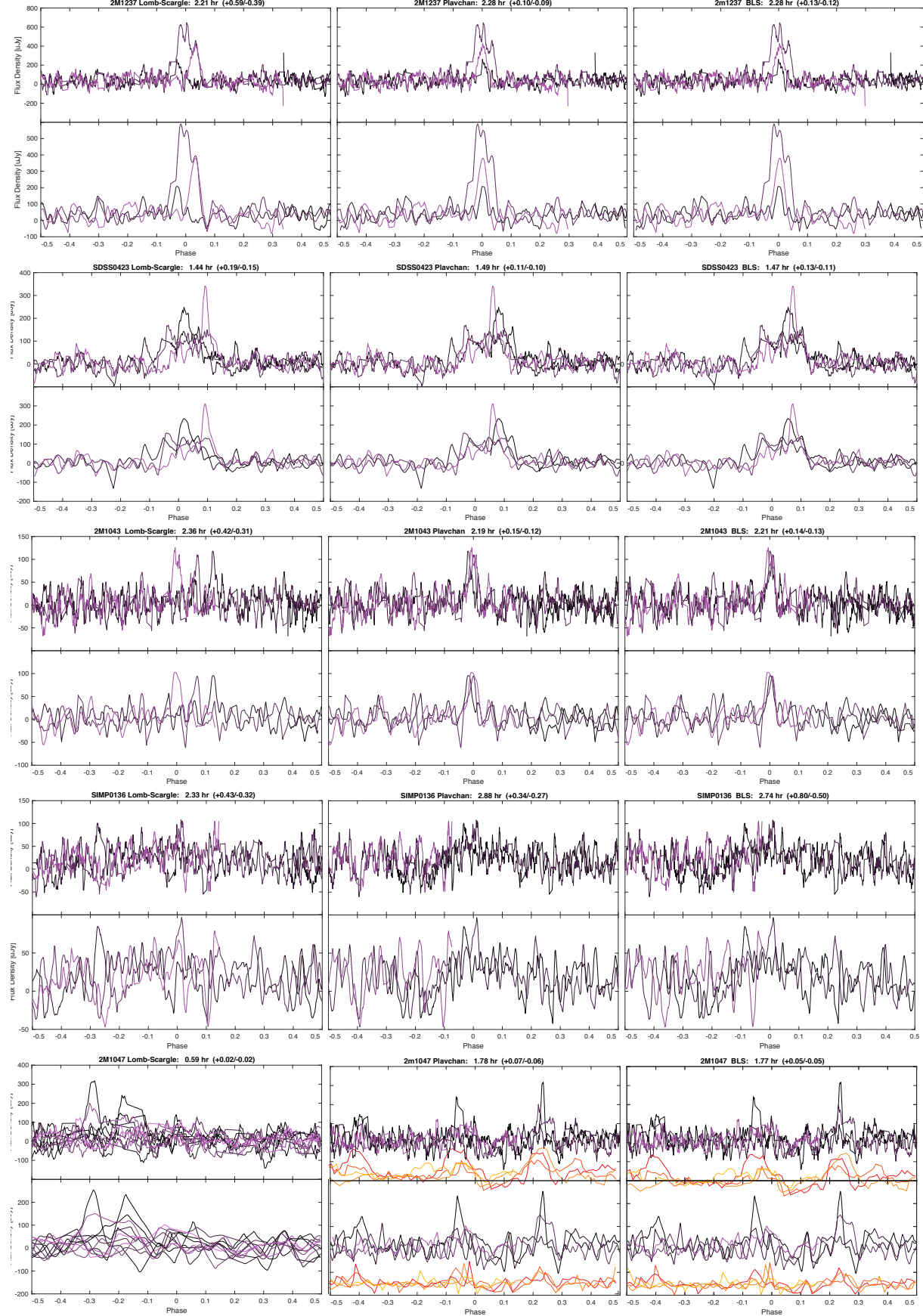


**Figure 6.** From left to right: Phase-folded 10s timeseries using periods from Lomb-Scargle (L-S), Plavchan, and Box-fitting Least Squares (BLS) periodograms. Top panels are raw data, bottom panels are smoothed data. 60s timeseries are overplotted in orange.

tational dynamics on convective flows (Gastine et al. 2013).

Complementing such models are sustained observational efforts to elucidate the effects of rotation on dynamo activity, in particular comparing magnetic activity tracers such as H $\alpha$  and X-ray emission to rotation rates or Rossby numbers (Pallavicini et al. 1981; Soderblom et al. 1993; Stauffer et al. 1994; Delfosse et al. 1998; Pizzolato et al. 2003; Reiners et al. 2009; McLean et al. 2012). The precipitous drop-off of X-ray emission from such objects indicate that the coolest brown dwarfs lack hot coronae, yet Zeeman broadening and Zeeman Doppler imaging observations confirm kilogauss fields. Previously established relationships between magnetic flux and tracers of coronal and chromospheric magnetic activity may not apply, calling for comparisons of direct magnetic field measurements rather than observational proxies to rotation rates. Radio brown dwarfs in particular provide a rich probe of rotationally dependent magnetism, since electron cyclotron maser emission frequencies map to field strengths, while rotational modulation of the emission can provide rotation period measurements.

We present here constraints on rotation periods for our objects. Our data are not sufficient to constrain models but may prove valuable in later detailed investigations into the effects of rotation on dynamo activity.

Our data are well-sampled with respect to pulse widths but very noisy and may contain low-amplitude or wide duty cycle peaks. Previous attempts have benefited from fitting the timeseries of relatively bright  $\sim$ mJy pulses (Hallinan et al. 2007, 2008; Williams & Berger 2015; Route & Wolszczan 2016), an order of magnitude brighter than the pulses in our targets. In contrast, for our data, some pulses do not become apparent until the data have been averaged to 60s or 120s resolutions, further introducing uncertainty when attempting to accurately identify pulses and their arrival times. For these reasons, we elected not to pursue a Levenberg-Marquardt or Monte Carlo time-of-arrival fitting (Williams & Berger 2015; Route & Wolszczan 2016) and instead employ three independent algorithms widely used in exoplanet transit and radial velocity searches. Using these algorithms has the added benefit of independently verifying the pulses that we identified in §4.2. The first is the classic Lomb-Scargle periodogram, which relies on decomposing timeseries into Fourier components and is optimized to identify sinusoidally-shaped periodic signals in time-series data, making this algorithm most appropriate for testing periodicity in broader pulses such as those observed in the SDSS0423 and SIMP0136 timeseries or even our

targets' quiescent emission. The second method is the Plavchan periodogram, a brute force method that derives periodicities in a method similar to that employed by phase dispersion minimization (Stellingwerf 1978), but circumvents period aliasing because it is binless (Plavchan et al. 2008; Parks et al. 2014). The Plavchan algorithm is not dependent on pulse shape and thus is sensitive to both sinusoid-dominated variability and other pulse profiles. Finally, the shapes of some of the pulses bear resemblance to inverse light curves of planet transits, for which the Box-fitting Least Squares (BLS) algorithm is optimized (Kovács et al. 2002).

We generate periodograms for all of our objects using the 10s time-averaged timeseries for the full bandwidth data and at all sub-bands using the MATLAB Lomb-Scargle function `plomb` and the NASA Exoplanet Archive Periodogram Service<sup>2</sup> for Plavchan and BLS periodograms. The Plavchan algorithm depends on two input parameters: number of outliers and fractional phase smoothing width, which we vary between 10%–30% of total data points and 0.025 - 0.1, respectively. BLS depends on three input parameters: number of points/bin, minimum fractional period coverage by pulse, and maximum fraction period coverage. For BLS, we hold the minimum fractional period coverage constant at 0.01, and we vary the number of points/bin and maximum fractional period coverage between 10–100 and 0.1–0.3, respectively. In most cases, the recovered periodicities do not depend much on these parameters and we discuss exceptions below.

We compare peaks with false alarm probability less than 10% returned by the the Lomb-Scargle algorithm to the most significant periods returned by the other algorithms in Figure 5 and visually inspect periods by phase-folding the timeseries in Figure 6 with the most significant period returned by each algorithm. In all cases except for 2M1047, periods returned by each algorithm are consistent within uncertainties, defined as the FWHM of the power peaks. We list periods returned by each algorithm in Table 9 and adopt the periods that result in the folded timeseries with the most visual agreement in pulse overlaps.

The data for 2M1237 do not appear to provide enough phase coverage to adequately sample periods longer than  $\sim$ 3.77 hours, with Plavchan peak power locations at and longer than this period changing dramatically depending on input variables and especially on the fractional amount of outliers. Specifically, the periodograms with a lower fraction of allowed outliers are biased in favor

<sup>2</sup> <https://exoplanetarchive.ipac.caltech.edu/cgi-bin/Pgram/nph-pgram>

of a period that is approximately twice that favored by periodograms with higher allowed outlier fractions because the large-amplitude pulse in the timeseries deviates strongly from the mean amplitude of the smaller pulses before and after it. Therefore, when the algorithm is not allowed to ignore points from this strong pulse, it will favor a rotation period that generates a timeseries akin to one with a main transit and a secondary eclipse. Additional phase coverage to characterize the variability behavior of the pulse profile is necessary to resolve the ambiguity between period harmonics.

A similar ambiguity exists for 2M1047. The Lomb-Scargle periodogram returns a  $\sim 0.59$  hr period, while Plavchan returns  $\sim 1.77$  hr, and BLS returns either  $\sim 3.54$  hr or  $\sim 1.77$  hr depending on the maximum allowed rotation pulse phase coverage and phase binning. Happily, these periods are all harmonics, indicating a non-spurious origin. Similar to 2M1237, the longest period is favored by the BLS algorithm for the cases with the least number of data points per bin, emphasizing the significance of the strongest peaks. The Plavchan periodogram also reflects this behavior, although its most significant period is consistently  $\sim 1.77$  hr irrespective of input parameters. For ground-based transit surveys, a typical number of points per bin is of order a few tens to a hundred, which would correspond to a  $\sim 1.77$  hr period. This period is consistent with that measured by [Williams & Berger \(2015\)](#) using 10-hr C-band (4–6 GHz) observations. We therefore adopt this period.

At  $\sim 2.88$  hr, the recovered periodicity for SIMP0136 is slightly longer than its  $\sim 2.4$  hr photometric periodicity and it appears to be based on the variability in the quasi-quiescent emission. However, we caution that our data has only a limited 7 hr baseline as compared to photometric studies, which span many hours over several nights, including a recent 18-night study ([Croll et al. 2016](#)). We analyzed the 4–8 GHz data and find that the C-band period appears consistent with  $\sim 2.88$  hr, but the data is even less conclusive since the total C-band observing block was only 4 hours long. The radio rotation period of Saturn has been observed to drift, but only by  $\sim 1\%$  ([Galopeau & Lecacheux 2000](#)). The nature of the quiescent component of brown dwarf radio emission remains unconfirmed (see §5.1), but the high degree of circular polarization observed in this component for SIMP0136 could indicate a coherent mechanism. If this is the case, we speculate that the difference in periods may be evidence of a moon interaction similar to the Io-Jupiter interaction, which produces an auroral ‘footprint’ that tracks the orbit of Io relative to Jupiter ([Ray & Ergun 2012](#)). Because the mechanism generating the non-pulsed but varying quiescent emission and

its location within the brown dwarf system remain unknown while the infrared variability is expected to occur within the brown dwarf atmosphere, we adopt the rotation period constrained by photometric studies for our discussion in §5.

Our data confirm that to date, all pulsing radio brown dwarfs with rotation period measurements have reported rotational periods between 1.77 and 3.89 hours ([Pineda 2016](#), and references therein). These rotation periods likely fall well within the limit of rapid rotation ( $Ro < 0.1$ ), with measured rotation periods on the order of just a few hours compared to convective turnover times that may be in the tens to hundreds of days (e.g. [Noyes et al. 1984](#); [Pizzolato et al. 2003](#); [McLean et al. 2012](#); [Landin et al. 2010](#)).

The previous statement comes with some important caveats. First, empirical estimations and numerical calculations of convective turnover times with observable properties such as X-ray luminosity do not extend to L and T dwarfs. Second, dynamo regions can span a wide range of fluid densities, with density stratification ranging from  $\sim 20\%$  in incompressible fluids such as in the geodynamo to at least  $\sim 10^6$ – $10^{10}$  in stars and likely also cool brown dwarfs ([Saumon et al. 1995](#)). In highly stratified regimes, fluids in the most diffuse regions become less efficient at transporting heat and small-scale motions with accompanying shorter convective turnover times may become increasingly important. Defining an appropriate Rossby number is not straightforward, since it is unclear where in the dynamo region is most important for generating fields that auroral radio emission probes. Finally, most brown dwarf radio detections have relied on short time baselines, biasing detections of radio brown dwarfs toward toward high rotation rates. This begs the question of whether rapid rotation rate is indeed important for generating strong large-scale kilogauss fields in the coolest brown dwarfs or is a requirement for driving auroral emissions or both. Continuing to push magnetic field measurements to higher frequencies with the goal of measuring true ECM cutoff frequencies will provide insight into how and whether field strengths empirically depend on rotation.

## 5. DISCUSSION

### 5.1. *The Curious Case of Highly Circularly Polarized and/or Disappearing Quiescent Emission*

[Kao et al. \(2016\)](#) noted that all previously detected radio brown dwarfs exhibited detectable levels of quiescent emission and [Pineda \(2016\)](#) showed that the quiescent radio luminosities correlated with H $\alpha$  luminosities for confirmed auroral emitters (i.e. with clear rotational modulation in the highly circularly polarized

emission component). This hinted of a connection between pulsed and quiescent radio processes. However, we do not observe detectable levels of quiescent emission from SDSS0423 and 2M1043 for 8–12 GHz or individual 1- or 2-GHz sub-bands, down to rms noise levels of  $\sim 1.7$ – $4.3 \mu\text{Jy}$  and  $\sim 1.2$ – $2.5 \mu\text{Jy}$ , respectively. We also do not observe detectable quiescent emission from 2M1047 at frequencies  $\gtrsim 13.5$  GHz down to rms noise levels of  $\sim 3.5$ – $5.2 \mu\text{Jy}$ .

For SDSS0423, Kao et al. (2016) measured a 4–8 GHz mean quiescent flux density of  $26.7 \pm 3.1 \mu\text{Jy}$ . Assuming an upper  $3\sigma$  detection limit of  $5.1 \mu\text{Jy}$  for flux density averaged over 8–12 GHz, the upper limit spectral index is  $\alpha \lesssim -3.2 \pm 0.7$  and the corresponding mildly relativistic power-law electron distribution index is  $\delta \gtrsim 5.0$ . For 2M1043, Kao et al. (2016) measured a 4–8 GHz mean quiescent flux density of  $16.3 \pm 2.5 \mu\text{Jy}$ , which leads to  $\alpha \lesssim -3.0 \pm 0.7$  and  $\delta \gtrsim 4.7$ . In the stellar case, typical spectral indices for quiescent radio emission from active M dwarfs are much flatter at  $\sim 0.3$  (e.g. Güdel et al. 1993; Güdel 1994, and references therein), though there may be fundamental differences for the brown dwarf case. While abundant evidence exists that much of the quiescent emission from ultracool dwarfs exhibits behavior consistent with incoherent synchrotron or gyrosynchrotron emission (e.g. Ravi et al. 2012; Williams et al. 2015), there have been some objects that depart from this model.

It is possible that at least some component of the ‘quiescent’ (non-pulsed) emission may be coherent, as the steep spectral index implied by the drop-off in quiescent emission is atypical (but not impossible) for non-thermal gyrosynchrotron or synchrotron emission (Dulk 1985; Melrose 2006) and may be more indicative of an emission cutoff. Such a model has been proposed for solar quiescent emission with electron power-law indices  $\delta \approx 2$ – $4$  and weak  $\sim 100$  G fields (Pallavicini et al. 1985; White et al. 1989; White & Franciosini 1995; Umana et al. 1998), including both plasma and gyrosynchrotron emission. Evidence for a coherent mechanism at play in the quiescent component precedes the data presented here. For instance, the L3.5 dwarf 2MASS J00361617+1821104 exhibits broadly varying emission with duty cycles  $\sim 30\%$  of the rotational period (Berger 2002; Hallinan et al. 2008). This emission could be decomposed to a periodic and highly circularly polarized component, which Hallinan et al. (2008) attributed to ECM, and also a component that was largely unpolarized for two out of three of the observed rotation periods. In the third rotation period, this component emitted two narrower peaks up to  $\sim 75\%$  right and left circular polarization, respectively. This same feature was observed in

data separated by 18 months, which demonstrated the longevity of this high degree of circular polarization and ruled out incoherent gyrosynchrotron as a mechanism. To explain the observed short-term variability in the degree of polarization, Hallinan et al. (2008) argued that local conditions in the emitting region could plausibly depolarize the emission, a phenomenon that commonly occurs in the strongly circularly polarized millisecond spikes of solar radio emission, such that polarization fractions can range from 0–10% (Benz 1986).

Similarly, Williams et al. (2016) reported emission varying over 20–40 min timescales in the T6 dwarf WISEP J112254.73+255021.5, including clear  $\sim 10$  min bursts in right circular polarization as well as a more broadly varying component and less clear variability in the left circularly polarized flux density, with spectral index  $\alpha = -1.5 \pm 0.3$ . Particularly noteworthy is the consistently high degree of circular polarization ( $> 50\%$ ) present for nearly the entire duration of their 162 min observation. This is similar to what we observe(d) in SIMP0136 and 2M1237, which have flatter spectra than SDSS0423 and 2M1043 if no variability is assumed, with spectral indices  $\alpha \approx -2.1 \pm 0.4$  and  $\alpha \approx -0.9 \pm 0.3$ , respectively. In contrast, Williams & Berger (2015) reported ‘quasi-quiescent’ emission from 2M1047 at 4–8 GHz that was not circularly polarized yet still showed evidence of possible variability with  $\sim 60 \mu\text{Jy}$  amplitude over a  $\sim 20$  min timescale and a flat spectral index of  $\alpha = 0.9 \pm 1.0$ . Kao et al. (2016) measured a 4–8 GHz mean quiescent flux density of  $17.5 \pm 3.6 \mu\text{Jy}$ , which leads to  $\alpha \approx -0.9 \pm 0.4$  and  $\delta \approx 2.4$ , when we take the 12–18 GHz mean quiescent flux density.

In the case that the non-pulsed emission is coherent, plasma emission is unlikely because the plasma density in a cool brown dwarf such as SDSS0423 is expected to be tenuous in comparison to the Solar corona, and the plasma frequency scales with the electron density as  $\nu_p \propto n_e^{1/2}$ . For a gas to exhibit plasma-like behaviors, electron-electron interactions should dominate over electron-neutral interactions. In models of thermal ionization for temperatures characteristic of M–T dwarfs, Rodriguez-Barrera et al. (2015) find that whereas M dwarfs can expect  $\sim 10^{-1}$  fraction of ionization in their atmospheres, this rapidly drops to  $\sim 10^{-4}$ – $10^{-3}$  for 1000 K objects. Additionally, the presence of plasma would correlate with X-ray emission, but L and later brown dwarfs remain underluminous in X-ray compared to their warmer counterparts (Williams et al. 2014). Finally, the free-free opacity  $\tau_{\text{ff}}$  for plasma emission is

$$\tau_{\text{ff}} = 46s^{-4}\nu_{p,\text{GHz}}^2 T_6^{-3/2} \left( \frac{H}{30 \text{ Mm}} \right), \quad (1)$$

where  $s$  is the emission harmonic (typically emitted at the fundamental or second harmonics),  $\nu_p$  is the plasma emission frequency for that harmonic,  $T$  is the temperature given in  $10^6$  K, and  $H$  is the density scale height along the emission path. In the Sun, which has coronal temperature  $\sim 10^6$  K, plasma emission is rarely observed above  $\sim 1$  GHz owing to strong reabsorption (Dulk 1985; Güdel 2002, and references therein). The other plausible coherent mechanism would be ECM emission in the form of superposed flares, as observed for 2MASS J00361617+1821104 (Hallinan et al. 2008). However, if the mechanism generating this quiescent emission is indeed related to the pulsed emission, the presence of the pulses observed in the same frequency bands would preclude the observed cutoff, unless the emitting regions traced different magnetic field strengths. This scenario could account for the strong circular polarization of the non-flaring emission from SIMP0136, 2M1237, and WISEP J112254.73+255021.5.

Another likely explanation is that the quiescent emission may exhibit long-term variability. Such variability has been previously reported in other brown dwarfs. For instance, Antonova et al. (2007) did not detect any radio emission from a 9 hr observation (with  $3\sigma$  upper limit  $\sim 45$   $\mu$ Jy) of 2MASS J05233822-1403022 (L2.5) on 2006 September 23, which Berger et al. (2010) also reported for observations on 30 December 2008. Archival data analyzed by Antonova et al. (2007) revealed that this same object was also not detected on 03 May 2004 with  $3\sigma$  upper limit of 42  $\mu$ Jy, yet it was detected sans flare on 17 May 2004 with flux density  $95 \pm 19$   $\mu$ Jy and also on 18 June 2004 with flux density  $230 \pm 17$   $\mu$ Jy, the latter of which was previously reported by Berger (2006). Similarly, Berger et al. (2010) reported no detectable emission from BRI 0021 (M9.5) with  $3\sigma$  upper limits of 54  $\mu$ Jy and 48  $\mu$ Jy for 4.9 GHz and 8.5 GHz, despite a previous marginal detection of its quiescent emission at  $40 \pm 13$   $\mu$ Jy as well as a flare with a peak flux density of  $360 \pm 70$   $\mu$ Jy. In the case that the quiescent emission is variable over longer timescales, long-term monitoring of radio brown dwarfs would be necessary to quantify how much the current detection rate underestimates the true detection rate and may warrant revisiting previously undetected objects with H $\alpha$  or infrared variability such as SDSS J12545393-0122474 (Kao et al. 2016).

The possible quiescent emission drop-off observed in SDSS0423 and the high degree of circular polarization in the non-pulsed emission from SIMP0136 and 2M1237 together highlight the question: Where is the line between pulsed and quiescent emission? Is it possible for ECM emission to also manifest as quiescent (not pulsed) emission?

## 5.2. Intermittent Pulses: Implications for ECM Emission Frequency Cutoff

At these high frequencies, pulses appear to be more intermittent compared to previous 4–8 GHz observations (Route & Wolszczan 2012; Williams & Berger 2015; Kao et al. 2016), with short-duration variability in both time and frequency. For instance, while the central pulse in 2M1237 is present at all bandwidths, the right-most peak is clearly apparent only at 11–12 GHz. In SDSS0423, there are two faint right-circularly polarized pulses in 8–9 GHz, but the right pulse appears to drop out at higher frequencies. In 2M1047, there appears to be a multi-peaked or long-lived left-circularly polarized pulse at 12.8–13.5 GHz early in the observing block that drops out at higher frequencies, only to be replaced by three fainter left-circularly polarized pulses distributed throughout the entire observing block. This is in contrast to these objects’ C-band (4–8 GHz) pulses, which Kao et al. (2016) reported to be present at all sub-bands.

This suggests that the conditions for current systems driving these auroral emissions may be much less stable or more variable close to the surface of the star, where fields are expected to be stronger. For instance, although large-scale fields appear necessary to drive Solar System auroral currents and the same may occur in isolated brown dwarfs such as our targets, as radiating electrons traverse these large-scale field lines inward, they will radiate at the frequencies corresponding to the magnetic fluxes that they see. Near the object surface, evolving and complex small-scale fields may also begin to emerge, and some fully convective dynamo models capable of generating kilogauss fields suggest that these small scale fields may be driven by convection near the surface, where convective turnover times are shorter and small-scale intermittent features begin to appear in convective flows. In contrast, more stable large-scale fields appear to be driven by slowly overturning convection in the deep interiors (Browning 2008).

Other examples of intermittent auroral pulse structures exist in the literature. As an example, the dynamic spectrum of LSR J1835+3259 shows one pulse per rotation extending through  $\sim 4$ –8 GHz, one extending through  $\sim 4$ –6 GHz, and one only extending through  $\sim 4.5$  GHz, with emission from each pulse appearing to fade away or renew again at different frequencies (Hallinan et al. 2015). Narrowband and intermittent pulses have also been observed in terrestrial, Jovian, and Saturnian auroral kilometric radiation (AKR). High-resolution dynamic spectra reveal that rather than one continuous pulse through frequency, AKR actually consists of many small-scale micropulses from individually radiating sources that are highly time variable and

narrowly-spaced in frequency, with widths of order  $\sim$ 10–1000 Hz corresponding to bunched groups of these local AKR sources traveling very rapidly through space. The origin of this fine structure remains unknown, but it is speculated that they may reflect a number of physical processes including propagation and absorption effects or small-scale field parallel current structures (Gurnett et al. 1981; Pottelette et al. 1999; Treumann 2006, and references therein).

While we do observe what appears to be the disappearance of highly circularly polarized pulsed auroral emission in SIMP0136, 2M1043, and SDSS0423 at 11–12 GHz, in light of the observed behavior in 2M1237 and 2M1047 and the above-discussed cases, we classify these dropoffs only as very tentative evidence of ECM emission cutoff. The known intermittent behavior of AKR suggests that observations through a much wider bandwidth of high frequencies are necessary to confirm a true emission cutoff.

### 5.3. Comparison to Luminosity-Driven Model

**Table 10.** Adopted Magnetic Fields

Object	Tentative $\nu_{\text{cutoff}}^{\text{a}}$ (GHz)	Local field $B_{\text{ECM}}^{\text{b}}$ (kG)	Min avg field $B_{\text{s,dip}}^{\text{c}}$ (kG)
2M1047	17.25	6.2	4.4
SIMP0136	10.5	3.7	2.7
2M1043	11.0	3.9	2.8
2M1237	11.5	4.1	2.9
SDSS0423	11.0	3.9	2.8

<sup>a</sup>Center of highest subband with imaging detection of ECM pulse.

<sup>b</sup> $B_{\text{ECM}} \text{ [kG]} = \nu_{\text{ECM}} \text{ [GHz]} / 2.8$  (Treumann 2006)

<sup>c</sup> $\langle B_{\text{s,dip}}^2 \rangle = \frac{1}{2} B_{\text{ECM}}^2$  (Kao et al. 2016)

Previously, Kao et al. (2016) found tentative evidence of a T dwarf departure from a predominantly luminosity-driven dynamo for rapid rotators ( $P < 4$  days). This model extended planetary dynamo models to stellar-mass objects including T Tauri stars and old M-dwarfs, whose Zeeman broadening and Zeeman Doppler imaging measurements appeared to be empirically consistent with a scaling relationship linking magnetic field strength to convected energy flux and dynamo density and largely independent of both magnetic

diffusivity and rotation rate (Christensen et al. 2009, hereafter C09). The broad span through planetary and stellar parameter spaces suggested that the scaling law may in fact present a unifying principle governing the magnetic field generation in all rapidly rotating, dipole-dominated fully convective objects – namely, that the bolometric flux  $q_0$  sets the magnetic field strength averaged over the whole volume of the dynamo region  $\langle B^2 \rangle$ , with a weak dependence on the mean density of the dynamo region  $\langle \rho \rangle$ :

$$\langle B^2 \rangle \propto \langle \rho \rangle^{1/3} q_0^{2/3}. \quad (2)$$

A previous lack of magnetic field measurements in the orders-of-magnitude mass and luminosity gap between planets and stars prevented further testing of this exciting model.

Several possible scenarios could explain the observed tentative inconsistency between late L and T dwarf magnetic fields with the C09 model, and we refer the reader to the discussion in Kao et al. (2016) §6.4. Of particular note is that the C09 model is specific to dipole-dominated fields ( $>35\%$  of field strength in the dipole component) in rapid rotators. It is therefore possible that higher order fields may dominate our objects. Without confirmed periods, an alternative was that several of our targets may be slower rotators.

Magnetic field topologies of our objects cannot be confirmed with only auroral radio emission, the frequency of which corresponds only to localized emitting regions in the magnetospheres of our targets. However, co-rotation breakdown models assuming Jovian-like ultracool dwarfs, with predominantly dipolar and axisymmetric magnetic fields and non-conducting atmospheres, show close agreement between modeled and observed auroral radio luminosities for TVLM 513-46546 (M9), LSR J1835+3259 (M8.5), and 2MASS J00361617+1821104 (L3.5) (Nichols et al. 2012). This model also predicted rotation periods between  $\sim 2.1$ – $2.8$  hr for 2M1047, which is not inconsistent with its measured rotation period. Additionally, while the exact nature of the electrodynamic engine — and therefore the magnetic field component powering the observed auroral emission — is not yet known, all of the known mechanisms for auroral emission in our Solar System rely on large-scale magnetic fields. Auroral emissions rely on coupling energy from locations where there is a large  $v \times B$  into the magnetosphere (Nichols et al. 2012). This is best achieved by having strong magnetic fields far away from the planet. Dipoles drop off much slower than higher order fields and almost always dominate auroral power for this reason. This suggests that auroral radio emission likely probes the

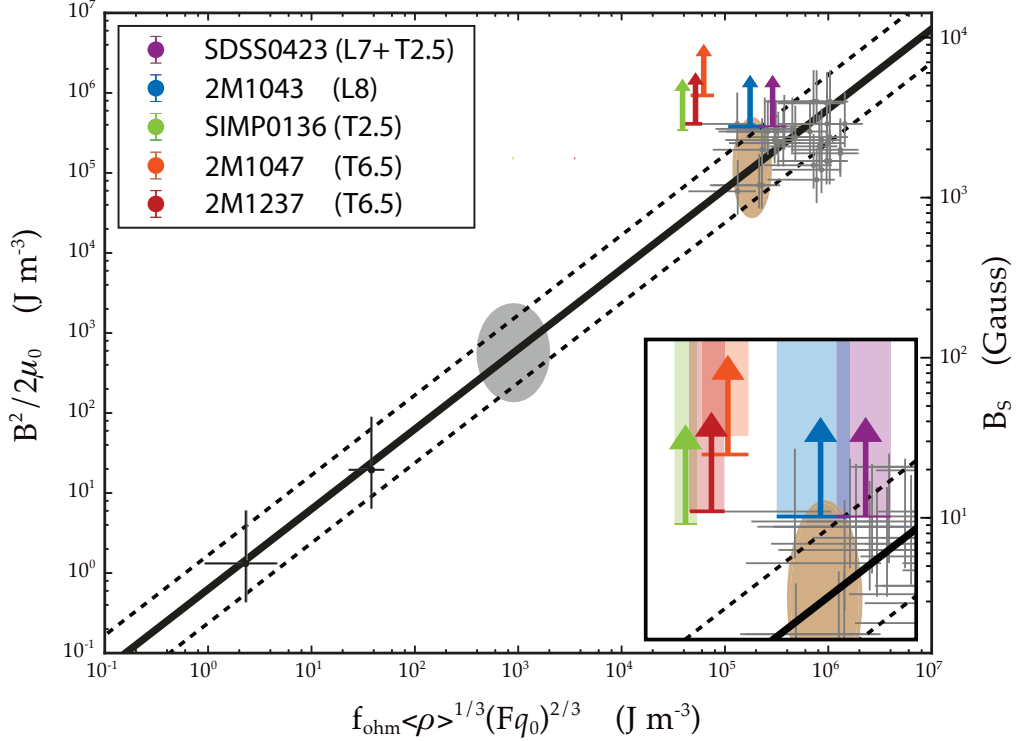


**Figure 7.** A comparison of estimated lower-bound magnetic field energy densities for our targets (overplotted arrows) to values predicted by the Christensen et al. (2009) scaling relation (black solid line) between convected energy density (x-axis,  $q_0$ ) and magnetic energy density (left y-axis) for fully convective dipole-dominated rapid rotators. Black dashed lines are  $3\sigma$  uncertainties on the model and horizontal bars on arrows are our estimated uncertainties. Previous constraints were T Tauri stars and old M dwarfs (gray crosses). Black points represent Earth and Jupiter. Brown and gray ellipses are predicted positions for a 1500 K brown dwarf and a  $7 M_J$  exoplanet, respectively. Right y-axis values are predicted surface-averaged fields  $B_s$ .

dipole components of our objects. Finally, ZDI studies indicate that fully convective M dwarfs appear to host  $\sim$ kG mean fields regardless of if they are dominated by dipole or higher-order fields, and dwarfs with kilogauss dipoles have order-of-magnitude weaker multipole fields and vice versa (Morin et al. 2010), making it unlikely that our targets have multipole-dominated fields if this behavior extends to L and T dwarfs. Indeed, even if the emergent structure in auroral emission discussed in §5.2 indicates the presence of small-scale fields near the brown dwarf surface, the largest scale fields still appear to store the most magnetic energy (Browning 2008). For a more detailed discussion of field topologies, we refer the reader to §6.3.1 in Kao et al. (2016).

Regarding the rapid rotation requirement for the C09 model, the periodicities that we recover in §4.3 unambiguously confirm that our targets are indeed rapid rotators, with rotation periods between  $\sim$ 1.44–2.88 hours. While SIMP0136 does not have any clearly periodic pulse structure, infrared cloud variability studies suggest a rotation period of  $2.3895 \pm 0.0005$  hr (Artigau et al. 2009; Croll et al. 2016). This rotation period is

slightly inconsistent with the recovered periodicity in its quasi-quiescent emission, which we measure to be  $2.88^{+0.34}_{-0.27}$  hr. Nevertheless, both periods fall well within the rapidly rotating regime such that  $Ro \ll 0.1$ .

Given the inconclusive evidence of ECM emission cut-off discussed in §5.2, we conservatively adopt ECM emission cutoff frequencies corresponding to the middle of the last sub-band with imaging detections of auroral pulses in Stokes I and V. Following the methodology outlined in Kao et al. (2016), we convert the local magnetic fields measured with ECM emission  $B_{\text{ECM}}$  to lower bound mean surface field magnitudes  $B_{s,\text{dip}}$  by assuming pure dipole fields for our objects, which we list in Table 10. As described in Kao et al. (2016),  $B_{s,\text{dip}}$  is equivalent to a lower bound Zeeman broadening measurement of a surface-averaged field strength  $B_s$ , and the presence of any higher-order fields would raise this estimate. We convert  $B_{s,\text{dip}}$  to a mean internal field strength  $\langle B \rangle$  for comparison to the C09 relation by following the conversions outlined in C09 and summarized in Kao et al. (2016).

We present our resulting field constraints on a reproduction of the C09 scaling law in Figure 7, with x-axis values determined from the physical parameters of our targets summarized in §2. The T dwarfs 2M1047, 2M1237, and SIMP0136 clearly depart by an order of magnitude from C09 magnetic energy predictions. While the late L dwarfs lie near the outer bounds of the  $3\sigma$  error on the scaling relationship, these are in fact conservative constraints; no emission frequency cutoff has been detected, pointing to the possibility of yet stronger fields. This tantalizingly hints at a possible ultracool brown dwarf locus that may not age along the predicted luminosity-magnetic field sequence (Reiners & Christensen 2010). Additional studies identifying aurorally pulsing radio brown dwarfs and characterizing their physical parameters could reveal such a locus.

#### 5.4. Consideration of Age-Related Models

The possibility that magnetic energy may scale with luminosity in rapidly rotating convective objects supports a picture in which brown dwarf magnetic fields are expected to decay with age as they cool through the L/T/Y spectral sequence and become increasingly less luminous. Indeed, field strengths can wane by a factor of 10% over the lifetime of a brown dwarf when evolutionary tracks are applied to the C09 model (Reiners & Christensen 2010).

The luminosity of a brown dwarf depends both on its age and its mass, and these factors may account for some of the possible emerging disagreement between the C09 relationship and our targets. Using the (Baraffe et al. 2003) brown dwarf evolutionary tracks and the C09 relationship, we calculated predicted age-evolving magnetic energy densities for each mass grid point and overplotted our objects in Figure 8. Given the disagreement between our objects and the C09 relation, it is no surprise that our objects also depart from these age-related predictions. However, while our T dwarf data appeared to disagree somewhat with the C09 model in §5.3, a departure was less clear for our L dwarfs. Accounting for the effects of age and mass on luminosity hints at a stronger departure from the Christensen et al. (2009) scaling law for our warmer but less massive and younger L dwarfs than was initially evident when mass and age were folded into luminosity. Regardless, a much larger sample is needed before any concrete conclusions can be drawn about how age affects convective dynamos, and the simplest prediction to test is whether objects with similar masses have stronger fields when younger.

In the event that luminosity ( $T_{\text{eff}}$ ) does not play a dominant role in brown dwarf dynamos, it is worth noting that magnetic field strengths do not appear to

vary much by age across an order of magnitude between  $\sim$ 200–3.4 Gyr. Of course, no definitive ECM emission cutoff frequency has been observed for any brown dwarfs yet, including our targets, so the plotted mean surface field strengths are merely lower bounds and the future addition of constraints from higher frequencies and a broader range of ages, masses, and temperatures may yet reveal a correlation between age and field strength.

Presenting our data within the context of age has an important implication for ongoing efforts to detect exoplanet radio emission. While such efforts have focused on hot Jupiters (which see high flux from host stars thus increasing the luminosity of solar-wind generated aurorae) and hot young exoplanets (Lazio & Farrell 2007; Lazio et al. 2010; Hallinan et al. 2013; Murphy et al. 2015; Lynch et al. 2017), old objects appear to also be capable of generating strong fields along with the associated radio emission, and broader searches may be warranted.

#### 5.5. First Radio Detection of Planetary-Mass Object?

Recently, Gagné et al. (2017) reported that the SIMP0136 may be a member of the  $\sim$ 200 Myr-old Carina-Near moving group based on its kinematics, with a field interloper probability of only 0.0001%. Using an empirical measurement of its bolometric luminosity and the the Saumon & Marley (2008) models, they inferred  $R = 1.22 \pm 0.01$  R<sub>J</sub>, which together predicted  $T_{\text{eff}} = 1098 \pm 6$  K and  $M = 12.7 \pm 1.0$  M<sub>J</sub>. New  $v \sin i$  measurements and its photometric periodicity constrained its inclination angle at  $i = 55.9_{-1.5}^{+1.6}$ °, giving a lower bound radius and corresponding upper bound on age and mass at  $R > 1.01 \pm 0.02$  R<sub>J</sub> and  $910_{-110}^{+26}$  Myr with  $M < 42.6_{-2.4}^{+2.5}$  M<sub>J</sub>. Models of the photometric variability assuming a single spot are in agreement, constraining its inclination at  $i < 60$ °, which would increase the lower bound radius to  $R > 1.17 \pm 0.02$  R<sub>J</sub>, further supporting the young age and low mass derived for SIMP0136 if it is indeed a member of the Carina-Near moving group.

With this new study, SIMP0136 may well be the first conclusively planetary-mass object with a radio detection, paving the way to testing planetary dynamos with hot young planetary-mass objects.

## 6. CONCLUSIONS

We detected auroral radio emission from four L7–T6.5 dwarfs up through 10–12 GHz, and one T6.5 object up through 15–16.5 GHz, corresponding to 3.7–5.6 kG local magnetic field strengths and 2.7–4.0 kG minimum surface averaged fields. Additionally, we reported a tentative 16.5–18 GHz auroral pulse detection for the T6.5

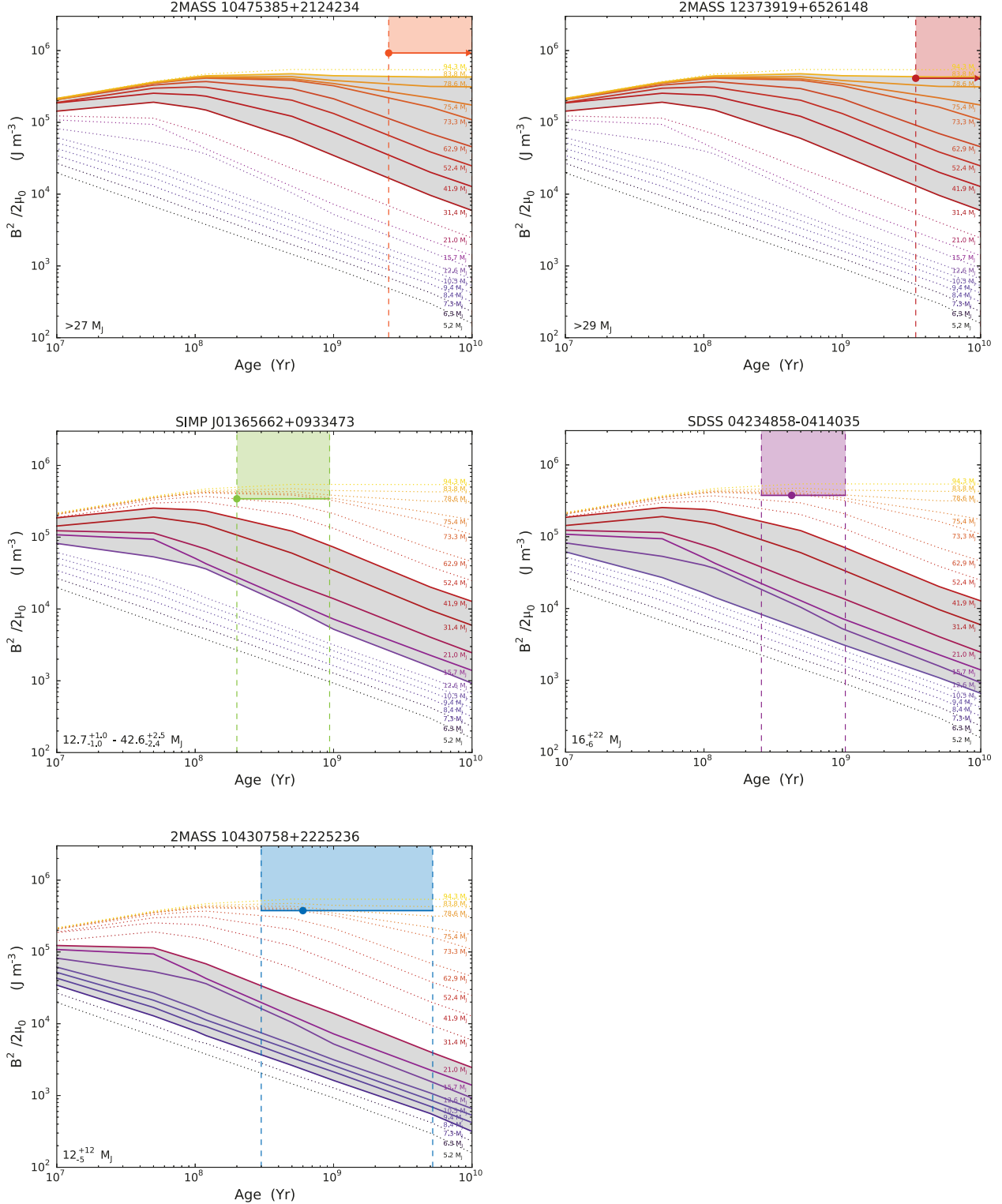


**Figure 8.** A comparison of estimated lower-bound magnetic field energy densities (colored circles) for our targets to magnetic energy density evolutionary tracks predicted using the dynamo scaling relationship from Christensen et al. (2009) and Baraffe et al. (2003) brown dwarf evolutionary tracks. Age uncertainties are shaded colored regions, which extend upward to indicate that magnetic field energy densities inferred from auroral radio magnetic field measurements are lower bounds. Age constraints for 2M1047 and 2M1237 give only lower bounds. Mass uncertainties are provided in bottom left corners, and corresponding mass tracks falling within these ranges (or those nearest the edge cases) are shaded in grey. For objects with only lower bound constraints on masses, we adopt  $0.08 M_{\odot}$  as the nominal hydrogen burning limit. The presence of strong  $\sim$ kilogauss fields across over an order of magnitude in ages is notable. Masses are adopted from Kao et al. (2016) and Gagné et al. (2017).

dwarf 2M1047, corresponding to 6.2 kG local magnetic field strengths and 4.4 kG minimum surface averaged fields. Pulses appear to be more intermittent in frequency at higher frequencies compared to previous observations of lower frequency counterparts, which can be interpreted as evidence of a higher degree of variability in the conditions necessary to generate auroral radio emission near the surfaces of brown dwarfs. While we observe the fading out of auroral pulses at 11–12 GHz for some targets, observations at higher frequencies are necessary to affirm definitive cut-offs in the auroral radio emission. We additionally observe no detectable quiescent emission for SDSS0423 but do observe highly circularly polarized non-pulsed emission from SIMP0136 and in some sub-bands also for 2M1237. The behavior of SDSS0423 may point to long term variability in the quiescent emission mechanism, while SIMP0136 and 2M1237 are more suggestive of coherent processes.

We have presented the strongest confirmed magnetic fields on the coolest brown dwarfs to date, representing the strongest direct constraints on dynamo theory at the substellar-planetary boundary. We have examined possible dynamo relationships depending on age and effective temperature. We presented data suggesting that a scaling relation between convected energy flux and magnetic energy density (Christensen et al. 2009) may not fit. Using the rotational modulation of auroral radio emission, we measured rotational periods between 1.47–2.88 hr. These short rotation periods are consistent with periods measured for earlier-type brown dwarfs using auroral radio emission and reiterates that rapid rotators can host strong large-scale fields. Finally, we find that our oldest targets (2M1047 and 2M1237, >2.5 Gyr) can generate fields that are as strong as those measured in our youngest targets ( $\sim$ 200–600 Myr), suggesting that old exoplanets may also host fields with strengths com-

parable to their younger siblings and serving as preliminary and very tentative evidence that age dependence in dynamo mechanisms may be weak. The absence of an emission frequency cut-off means that we have not broken any degeneracies in our analyses and a larger, more characterized sample is required.

Included in our sample was the archetypal cloud variable SIMP0136, which was recently found to be a member of a nearby  $\sim$ 200 Myr moving group. This new constraint reduces its estimated mass to a mere  $12.7 \pm 1.0 M_J$ , possibly making SIMP0136 the first known planetary mass object detected in the radio. If SIMP0136 is indeed a field exoplanet, its detection demonstrates that auroral radio emission can open a new avenue to detecting exoplanets, including elusive rogue planets.

## 7. ACKNOWLEDGEMENTS

MMK thanks Jackie Villadsen for helping to troubleshoot calibrations and Rakesh Yadav for thoughtful and instructive discussions about dynamo modeling.

This publication makes use of data products from the Two Micron All Sky Survey, which is a joint project of the University of Massachusetts and the Infrared Processing and Analysis Center/California Institute of Technology, funded by the National Aeronautics and Space Administration and the National Science Foundation.

The National Radio Astronomy Observatory is a facility of the National Science Foundation operated under cooperative agreement by Associated Universities, Inc.

MMK was supported by the NRAO Grote Reber Doctoral Fellowship. JSP was supported by a grant from the National Science Foundation Graduate Research Fellowship under grant no. DGE-1144469.

*Facility:* JVLA

## REFERENCES

Antonova, A., Doyle, J. G., Hallinan, G., Golden, A., & Koen, C. 2007, *A&A*, 472, 257

Antonova, A., Hallinan, G., Doyle, J. G., et al. 2013, *A&A*, 549, A131

Apai, D., Radigan, J., Buenzli, E., et al. 2013, *ApJ*, 768, 121

Artigau, É., Bouchard, S., Doyon, R., & Lafrenière, D. 2009, *ApJ*, 701, 1534

Artigau, É., Doyon, R., Lafrenière, D., et al. 2006, *ApJL*, 651, L57

Artigau, E., Nadeau, D., & Doyon, R. 2003, in IAU Symposium, Vol. 211, Brown Dwarfs, ed. E. Martin, 451

Badman, S. V., Branduardi-Raymont, G., Galand, M., et al. 2015, *SSRv*, 187, 99

Baraffe, I., Chabrier, G., Barman, T. S., Allard, F., & Hauschildt, P. H. 2003, *A&A*, 402, 701

Batygin, K., & Stevenson, D. J. 2010, *ApJL*, 714, L238

Benz, A. O. 1986, *SoPh*, 104, 99

Berger, E. 2002, *ApJ*, 572, 503

—. 2006, *ApJ*, 648, 629

Berger, E., Ball, S., Becker, K. M., et al. 2001, *Nature*, 410, 338

Berger, E., Rutledge, R. E., Reid, I. N., et al. 2005, *ApJ*, 627, 960

Berger, E., Rutledge, R. E., Phan-Bao, N., et al. 2009, *ApJ*, 695, 310

Berger, E., Basri, G., Fleming, T. A., et al. 2010, *ApJ*, 709, 332

Brain, D. A., McFadden, J. P., Halekas, J. S., et al. 2015, *Geophys. Res. Lett.*, 42, 9142

Browning, M. K. 2008, *ApJ*, 676, 1262

Burgasser, A. J. 2007, *ApJ*, 659, 655

Burgasser, A. J., Burrows, A., & Kirkpatrick, J. D. 2006a, *ApJ*, 639, 1095

Burgasser, A. J., Geballe, T. R., Leggett, S. K., Kirkpatrick, J. D., & Golimowski, D. A. 2006b, *ApJ*, 637, 1067

Burgasser, A. J., Kirkpatrick, J. D., Liebert, J., & Burrows, A. 2003, *ApJ*, 594, 510

Burgasser, A. J., Kirkpatrick, J. D., Reid, I. N., et al. 2000, *AJ*, 120, 473

Burgasser, A. J., Liebert, J., Kirkpatrick, J. D., & Gizis, J. E. 2002, *AJ*, 123, 2744

Burgasser, A. J., Reid, I. N., Leggett, S. K., et al. 2005, *ApJL*, 634, L177

Burgasser, A. J., Kirkpatrick, J. D., Brown, M. E., et al. 1999, *ApJL*, 522, L65

Burgasser, A. J., Gillon, M., Faherty, J. K., et al. 2014, *ApJ*, 785, 48

Carson, J. C., Marengo, M., Patten, B. M., et al. 2011, *ApJ*, 743, 141

Chabrier, G., & Küker, M. 2006, *A&A*, 446, 1027

Charbonneau, P. 2005, *Living Reviews in Solar Physics*, 2, 2

Christensen, U. R., & Aubert, J. 2006, *Geophysical Journal International*, 166, 97

Christensen, U. R., Holzwarth, V., & Reiners, A. 2009, *Nature*, 457, 167

Clarke, F. J., Hodgkin, S. T., Oppenheimer, B. R., Robertson, J., & Haubois, X. 2008, *MNRAS*, 386, 2009

Croll, B., Muirhead, P. S., Lichtman, J., et al. 2016, *ArXiv e-prints*, arXiv:1609.03587

Cruz, K. L., Reid, I. N., Liebert, J., Kirkpatrick, J. D., & Lowrance, P. J. 2003, *AJ*, 126, 2421

Cruz, K. L., Reid, I. N., Kirkpatrick, J. D., et al. 2007, *AJ*, 133, 439

Delfosse, X., Forveille, T., Perrier, C., & Mayor, M. 1998, *A&A*, 331, 581

Donati, J.-F., Forveille, T., Collier Cameron, A., et al. 2006, *Science*, 311, 633

Duarte, L. D. V., Gastine, T., & Wicht, J. 2013, *Physics of the Earth and Planetary Interiors*, 222, 22

Duarte, L. D. V., Wicht, J., & Gastine, T. 2016, *ArXiv e-prints*, arXiv:1612.02870

Dulk, G. A. 1985, *ARA&A*, 23, 169

Durney, B. R. 1981, *ApJ*, 244, 678

Enoch, M. L., Brown, M. E., & Burgasser, A. J. 2003, *AJ*, 126, 1006

Gagné, J., Faherty, J. K., Burgasser, A. J., et al. 2017, *ApJL*, 841, L1

Galoapeau, P. H. M., & Lecacheux, A. 2000, *J. Geophys. Res.*, 105, 13089

Gastine, T., Duarte, L., & Wicht, J. 2012, *A&A*, 546, A19

Gastine, T., Morin, J., Duarte, L., et al. 2013, *A&A*, 549, L5

Gastine, T., Wicht, J., Duarte, L. D. V., Heimpel, M., & Becker, A. 2014, *Geophys. Res. Lett.*, 41, 5410

Güdel, M. 1994, *ApJS*, 90, 743

Güdel, M. 2002, *ARA&A*, 40, 217

Güdel, M., & Benz, A. O. 1993, *ApJL*, 405, L63

Güdel, M., Schmitt, J. H. M. M., Bookbinder, J. A., & Fleming, T. A. 1993, *ApJ*, 415, 236

Gurnett, D. A., Kurth, W. S., & Scarf, F. L. 1981, *Nature*, 292, 733

Hallinan, G., Antonova, A., Doyle, J. G., et al. 2006, *ApJ*, 653, 690

—. 2008, *ApJ*, 684, 644

Hallinan, G., Sirothia, S. K., Antonova, A., et al. 2013, *ApJ*, 762, 34

Hallinan, G., Bourke, S., Lane, C., et al. 2007, *ApJL*, 663, L25

Hallinan, G., Littlefair, S. P., Cotter, G., et al. 2015, *Nature*, 523, 568

Harding, L. K., Hallinan, G., Boyle, R. P., et al. 2013, *ApJ*, 779, 101

Hartmann, L., Herczeg, G., & Calvet, N. 2016, *ARA&A*, 54, 135

Johns-Krull, C. M., & Valenti, J. A. 1996, *ApJL*, 459, L95

Johns-Krull, C. M., & Valenti, J. A. 2000, in *Astronomical Society of the Pacific Conference Series*, Vol. 198, *Stellar Clusters and Associations: Convection, Rotation, and Dynamos*, ed. R. Pallavicini, G. Micela, & S. Sciortino, 371

Kao, M. M., Hallinan, G., Pineda, J. S., et al. 2016, *ApJ*, 818, 24

Kervella, P., Mérand, A., Ledoux, C., Demory, B.-O., & Le Bouquin, J.-B. 2016, *ArXiv e-prints*, arXiv:1607.04351

Kirkpatrick, J. D., Cruz, K. L., Barman, T. S., et al. 2008, *ApJ*, 689, 1295

Kovács, G., Zucker, S., & Mazeh, T. 2002, *A&A*, 391, 369

Landin, N. R., Mendes, L. T. S., & Vaz, L. P. R. 2010, *A&A*, 510, A46

Lazio, T. J., Carmichael, S., Clark, J., et al. 2010, *AJ*, 139, 96

Lazio, T. J., & Farrell, W. M. 2007, *ApJ*, 668, 1182

Leblanc, F., Modolo, R., Curry, S., et al. 2015, *Geophys. Res. Lett.*, 42, 9135

Liebert, J., & Burgasser, A. J. 2007, *ApJ*, 655, 522

Lynch, C. R., Murphy, T., Kaplan, D. L., Ireland, M., & Bell, M. E. 2017, *MNRAS*, 467, 3447

Marley, M. S., Saumon, D., & Goldblatt, C. 2010, *ApJL*, 723, L117

McLean, M., Berger, E., & Reiners, A. 2012, *ApJ*, 746, 23

Melrose, D. B. 2006, *ApJ*, 637, 1113

Miles-Páez, P. A., Metchev, S. A., Heinze, A., & Apai, D. 2017, *ApJ*, 840, 83

Moffatt, H. K. 1978, Magnetic field generation in electrically conducting fluids

Mohanty, S., & Basri, G. 2003, *ApJ*, 583, 451

Mohanty, S., Basri, G., Shu, F., Allard, F., & Chabrier, G. 2002, *ApJ*, 571, 469

Morin, J., Donati, J.-F., Petit, P., et al. 2010, *MNRAS*, 2269

Murphy, T., Bell, M. E., Kaplan, D. L., et al. 2015, *MNRAS*, 446, 2560

Nichols, J. D., Burleigh, M. R., Casewell, S. L., et al. 2012, *ApJ*, 760, 59

Noyes, R. W., Hartmann, L. W., Baliunas, S. L., Duncan, D. K., & Vaughan, A. H. 1984, *ApJ*, 279, 763

Olson, P., & Christensen, U. R. 2006, *Earth and Planetary Science Letters*, 250, 561

Pallavicini, R., Golub, L., Rosner, R., et al. 1981, *ApJ*, 248, 279

Pallavicini, R., Willson, R. F., & Lang, K. R. 1985, *A&A*, 149, 95

Parks, J. R., Plavchan, P., White, R. J., & Gee, A. H. 2014, *ApJS*, 211, 3

Perley, R. A., & Butler, B. J. 2013, *ApJS*, 204, 19

Pineda, J. S. 2016, PhD thesis, California Institute of Technology, doi:10.7907/Z90C4SRW

Pineda, J. S., Hallinan, G., Kirkpatrick, J. D., et al. 2016, *ApJ*, 826, 73

Pizzolato, N., Maggio, A., Micela, G., Sciortino, S., & Ventura, P. 2003, *A&A*, 397, 147

Plavchan, P., Jura, M., Kirkpatrick, J. D., Cutri, R. M., & Gallagher, S. C. 2008, *ApJS*, 175, 191

Pottelette, R., Ergun, R. E., Treumann, R. A., et al. 1999, *Geophys. Res. Lett.*, 26, 2629

Radigan, J. 2014, *ApJ*, 797, 120

Radigan, J., Lafrenière, D., Jayawardhana, R., & Artigau, E. 2014, *ApJ*, 793, 75

Ray, L. C., & Ergun, R. E. 2012, Washington DC American Geophysical Union Geophysical Monograph Series, 197, doi:10.1029/2011GM001172

Reiners, A. 2012, *Living Reviews in Solar Physics*, 9, 1

Reiners, A., & Basri, G. 2006, *ApJ*, 644, 497

—. 2007, *ApJ*, 656, 1121

—. 2008, *ApJ*, 684, 1390

—. 2009, *A&A*, 496, 787

—. 2010, *ApJ*, 710, 924

Reiners, A., Basri, G., & Browning, M. 2009, *ApJ*, 692, 538

Reiners, A., & Christensen, U. R. 2010, *A&A*, 522, A13

Rodríguez-Barrera, M. I., Helling, C., Stark, C. R., & Rice, A. M. 2015, *MNRAS*, 454, 3977

Rosén, L., Kochukhov, O., & Wade, G. A. 2015, *ArXiv e-prints*, arXiv:1504.00176

Route, M. 2016, *ArXiv e-prints*, arXiv:1609.07761

Route, M., & Wolszczan, A. 2012, *ApJL*, 747, L22

—. 2016, *ApJL*, 821, L21

Saumon, D., Chabrier, G., & van Horn, H. M. 1995, *ApJS*, 99, 713

Saumon, D., & Marley, M. S. 2008, *ApJ*, 689, 1327

Schmidt, S. J., Hawley, S. L., West, A. A., et al. 2015, *AJ*, 149, 158

Schmidt, S. J., West, A. A., Hawley, S. L., & Pineda, J. S. 2010, *AJ*, 139, 1808

Schmitt, J. H. M. M., & Rosso, C. 1988, *A&A*, 191, 99

Shulyak, D., Reiners, A., Wende, S., et al. 2010, *A&A*, 523, A37

Skrutskie, M. F., Cutri, R. M., Stiening, R., et al. 2006, *AJ*, 131, 1163

Soderblom, D. R., Stauffer, J. R., Hudon, J. D., & Jones, B. F. 1993, *ApJS*, 85, 315

Sreenivasan, B., & Jones, C. A. 2006, *Geophysical Journal International*, 164, 467

Stauffer, J. R., Caillault, J.-P., Gagne, M., Prosser, C. F., & Hartmann, L. W. 1994, *ApJS*, 91, 625

Steenbeck, M., & Krause, F. 1966, *Zeitschrift Naturforschung Teil A*, 21, 1285

Stellingwerf, R. F. 1978, *ApJ*, 224, 953

Treumann, R. A. 2006, *A&A Rv*, 13, 229

Ulmschneider, P. 2003, in *Lecture Notes in Physics*, Berlin Springer Verlag, Vol. 619, *Lectures on Solar Physics*, ed. H. M. Antia, A. Bhatnagar, & P. Ulmschneider, 232

Umana, G., Trigilio, C., & Catalano, S. 1998, *A&A*, 329, 1010

Valenti, J. A., Marcy, G. W., & Basri, G. 1995, *ApJ*, 439, 939

Vernazza, J. E., Avrett, E. H., & Loeser, R. 1981, *ApJS*, 45, 635

Vidotto, A. A., Jardine, M., Morin, J., et al. 2013, *A&A*, 557, A67

Vrba, F. J., Henden, A. A., Luginbuhl, C. B., et al. 2004, *AJ*, 127, 2948

Weinberger, A. J., Boss, A. P., Keiser, S. A., et al. 2016, *AJ*, 152, 24

White, S. M., & Franciosini, E. 1995, *ApJ*, 444, 342

White, S. M., Kundu, M. R., & Jackson, P. D. 1989, *A&A*, 225, 112

Williams, P. K. G., & Berger, E. 2015, ArXiv e-prints, arXiv:1502.06610

Williams, P. K. G., Berger, E., & Zauderer, B. A. 2013, *ApJL*, 767, L30

Williams, P. K. G., Cook, B. A., & Berger, E. 2014, *ApJ*, 785, 9

Williams, P. K. G., Gizis, J. E., & Berger, E. 2016, ArXiv e-prints, arXiv:1608.04390

Wilson, P. A., Rajan, A., & Patience, J. 2014, *A&A*, 566, A111

Yadav, R. K., Christensen, U. R., Morin, J., et al. 2015, *ApJL*, 813, L31

Yadav, R. K., Christensen, U. R., Wolk, S. J., & Poppenhaeger, K. 2016, *ApJL*, 833, L28

Zarka, P. 1998, *J. Geophys. Res.*, 103, 20159